Estimate of the aerosol properties over the ocean with POLDER

J. Deuzé, P. Goloub, M. Herman, A. Marchand, G. Perry, S. Susana, D. Tanré

JOURNAL OF GEOPHYSICAL RESEARCH, VOL. 105, NO. D12, PAGES 15,329–15, 346, JUNE 27, 2000

Estimate of the aerosol properties over the ocean with POLDER

J. L. Deuzé, P. Goloub, M. Herman, A. Marchand, and G. Perry

Laboratoire d'Optique Atmosphérique, Université de Lille 1, Villeneuve d'Ascq, France

S. Susana

Laboratoire des Sciences du Climat et de l'Environnement, Commissariat à l'Energie Atomique Saclay, Gif-sur-Yvette, France

D. Tanré

Laboratoire d'Optique Atmosphérique, Université de Lille 1, Villeneuve d'Ascq, France

Abstract. The wide field of view imaging spectroradiometer Polarization and Directionality of the Earth's Reflectance (POLDER) developed by Centre National d'Etudes Spatiales and operated aboard the Japanese heliosynchronous platform Advanced Earth Observation Satellite (ADEOS) from October 30, 1996, to June 30, 1997, provided the first global systematic measurements of the spectral, directional, and polarized characteristics of the solar radiation reflected by the Earth/atmosphere system. These original observational capabilities offer an opportunity to enhance the characterization of several components of the global environment, especially the oceanic and terrestrial vegetal primary production, the aerosol physical and optical properties, and the tridimensional structure and microphysics of clouds. Here we examine the remote sensing of aerosols over the oceans. In a first step the aerosol optical thickness and Ångström exponent are derived from the radiance measurements. In a second step the polarization measurements are used for the retrieval of the aerosol refractive index. The inversion algorithm assumes spherical, nonabsorbing particles with monomodal lognormal size distribution. The adequacy of this modeling is discussed for a representative set of aerosol observations. Successful retrieval is generally achieved in the presence of small aerosols with Ångström exponent larger than ~1.0. For such particles, polarization may provide information on the particle refractive index. As the Ångström exponent of the particle decreases, the data fitting residual errors increase, especially in polarized light, which prevents the retrieval of the aerosol refractive index. The trends of the discrepancies point out two shortcomings of the aerosol modeling. The theoretical results systematically underestimate the contribution of small polarizing particles in the polarization measurements for side-scattering angles ranging from 80° to 120°. This indicates very probably that aerosol models have to follow bimodal size distribution. On the other hand, the systematic trend of the directional behavior of the upward radiance and the lack of significant rainbow effect in the measurements result probably from nonsphericity of some large aerosols. Confirmation of these points requires improved analysis of the POLDER data.

1. Introduction

Although minor constituent of the atmosphere, aerosols are known to contribute substantially to climate forcing and geochemical cycles [*Hansen and Lacis*, 1990; *Charlson et al.*, 1992], and there is increasing interest in their global distribution. Many efforts have been devoted to remote sensing of the aerosols from Earth-orbiting satellites [*Fraser*, 1976; *Quenzel and Koepke*, 1984; *Rao et al.*, 1989; *Higurashi and Nakajima*, 1999]. Global maps of the aerosol content over the ocean are presently derived routinely from National Oceanic and Atmospheric Administration and advanced very high resolution radiometer (NOAA AVHRR) data [*Stowe et al.*, 1992; *Husar et al.*, 1997] by using a one-channel algorithm, which needs the choice of a mean aerosol model. Moreover, qualitative monitoring of UV-absorbing aerosols, both over land and ocean, has been achieved recently by using the ultraviolet measurements of the Total Ozone Mapping Spectrometer (TOMS) on Nimbus 7 [*Herman et al.*, 1997; *Torres et al.*, 1998]. Given the large variability of the aerosol physical and chemical properties, improved characterization of the particles is a key issue for new remote sensing instruments, like Polarization and Directionality of the Earth's Reflectance (POLDER) and the Ocean Color Temperature Scanner (OCTS) [*Nakajima et al.*, 1999] on the Japanese ADEOS platform, the NASA's Sea-viewing Wide Field-of-view Sensor (SeaWiFS) [*Gordon and Wang*, 1994] and the Moderate Resolution Imaging Spectroradiometer (MODIS) on the NASA Earth Observing System (EOS) [*Tanré et al.*, 1997].

Paper number 2000JD900148.
0148-0227/00/2000JD900148$09.00

The wide field of view imaging spectroradiometer POLDER performs multispectral observations of the directionality and polarization of the solar radiation reflected by the Earth. Wide field of view optics and a matrix array detector provide both along- and cross-track viewing directions, so that the same terrestrial target can be observed from different viewing geometries during the same orbit. A rotating filter wheel provides radiance measurements in nine channels, ranging from 443 to 910 nm. Moreover, the channels centered at 443, 670, and 865 nm are equipped with polaroids, which permits measurements of the polarized light [*Deschamps et al.*, 1994]. These unique capabilities are expected to allow better characterization of different geophysical parameters concerning the terrestrial biosphere, the cloud radiative impact, and the ocean color. Particularly, they should offer new possibilities for characterizing the terrestrial aerosols from space.

POLDER was operating successfully aboard ADEOS from October 30, 1996, to June 30, 1997. The data have been processed by using inversion algorithms which were developed before the POLDER launch and implemented at the POLDER Processing Center, except for minor adjustments after the launch. The various POLDER geophysical products obtained by this way are available from the POLDER Processing Center at Centre National d'Etudes Spatiales (CNES). We address here the retrieval of the aerosol properties over the oceans. They consist of the aerosol optical thickness for wavelength λ_0 = 865 nm, δ_0, Ångström exponent, α, and refractive index, m, where α and m are column-averaged values. A preliminary validation of the δ_0 and α retrievals has been achieved [*Goloub et al.*, 1999], and preliminary results have been published [*Deuzé et al.*, 1999]. The object of this paper is to detail the inversion algorithm, to examine its performances and limitations, and to discuss the specific problems linked to the polarization analysis.

The main lines of the inversion scheme are described in section 2. The algorithm assumes spherical, nonabsorbing particles with single lognormal size distribution. In a first step the retrieval of δ_0 and α is achieved using only the radiance measurements in two aerosol channels. In a second step the refractive index retrieval is attempted from the polarization measurements. The algorithm performances are examined in section 3. The residuals of the experimental data fitting by the theoretical models are analyzed for a representative sample of aerosol observations. In section 4 the limitations of the present algorithm with respect to the aerosol modeling are discussed.

2. Principle of the Aerosol Algorithm

2.1. POLDER Data

The processing line starts from the POLDER level 1 data for each POLDER ground pixel. A pixel size of 6 km × 6 km is obtained after resampling on a latitude-longitude predefined grid. The data are multispectral radiances and polarized radiances at the top of the atmosphere (TOA) measured in 13 or 14 different viewing directions. The POLDER data are normalized radiances, $L_\lambda = \pi L^*_\lambda / E_s$, where E_s is the solar irradiance at TOA and L^*_λ is the radiance; λ is the central wavelength of the channel. The aerosol retrieval over the oceans is based on measurements in the two near-infrared channels centered at λ_0 = 865 nm and λ_1 = 670 nm, where the water-leaving radiance is negligible. Measurements at shorter wavelengths, especially in the 443-nm channel, are discarded because of the possible significant contribution of the water-leaving radiance.

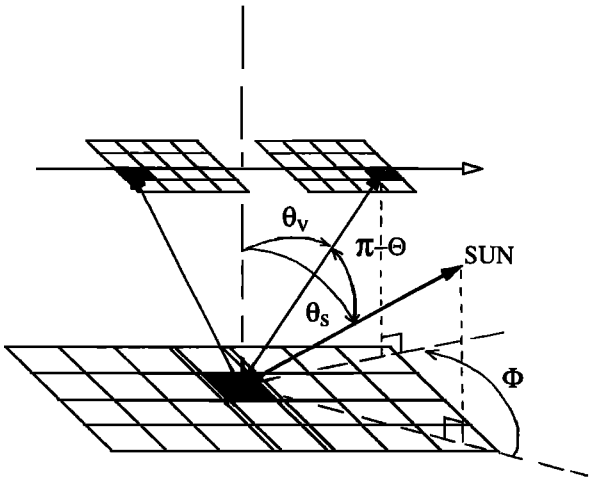

Figure 1a. Schematic of the POLDER imaging mode. The CCD matrix and the positions of the images of the same ground target are shown for two successive snapshots. The target is observed from zenith viewing angle, θ_v, and viewing azimuth angle, ϕ, which change according to the snapshot. A ground target appears in ~13 successive snapshots during the same orbit.

Cloud-free POLDER pixels are first selected according to the cloud-screening algorithm of *Bréon and Colzy* [1999], which is based on thresholds on the reflectance in the 443-nm channel, examination of the surface pressure derived from the POLDER channels centered in the oxygen absorption band, and seeking the presence of the rainbow arising from liquid clouds. The O_3 abundance derived from TOMS is used for correcting the 670-nm channel data for the ozone absorption. The H_2O content derived from the POLDER measurements in the 910-nm and 865-nm channels [*Vesperini et al.*, 1999] is used for correcting the 865-nm channel data for the water vapor absorption. Finally, the data are corrected for the stratospheric aerosol contribution using radiative transfer computations of this effect. The computations were based on a standard modeling of the stratospheric aerosols, with the global distribution of the aerosol optical thickness derived from a 2-year analysis of Stratospheric Aerosol and Gas Experiment (SAGE) II data [*Lafrance and Herman*, 1998]. Thus the inputs of the aerosol algorithm are cloud-free pixels corrected for gaseous and stratospheric contaminations. Moreover, 3 × 3 POLDER pixels (i.e., about 20 km × 20 km areas) are considered to reduce the noise level. The noise equivalent differential polarized radiance, $\mathrm{NED}L^p_\lambda$, is about 1.25×10^{-3} in level 1 data [*Hagolle et al.*, 1999; *Nadal*, 1999], that is, about 4×10^{-4} for the 3 × 3 pixels used here.

Although the algorithm takes into account the reflection from the sea surface, we select measurements in viewing directions where the sun glint contribution is negligible. The POLDER viewing geometry is illustrated in Figures 1a and 1b. Figure 1a is a schematic three-dimensional (3-D) illustration of the POLDER imaging mode. Figure 1b shows in polar coordinates the sampling of the bidirectional reflectance of the surface target according to the location of the target within the POLDER swath. The corresponding scattering angles are indicated. The radiance of the sun glint is estimated by using the *Cox and Munk* [1954] modeling of the rough sea surface, and

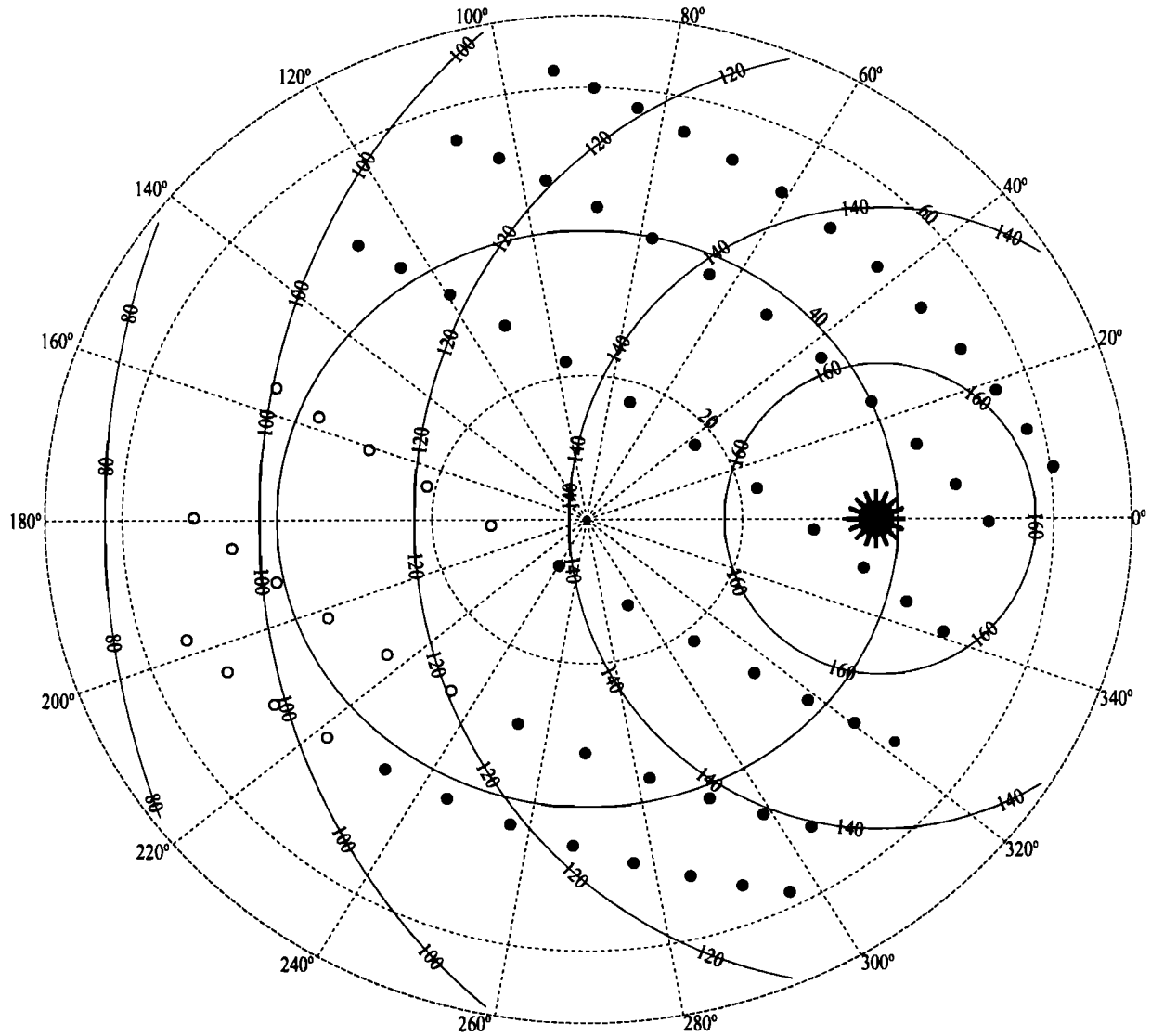

Figure 1b. Typical sampling of the bidirectional properties of the atmosphere from POLDER. The target latitude is 20°N, the solar zenith angle is 38°. The target viewing directions are reported in a (θ_v, ϕ) polar diagram (radius is viewing zenith angle; angle is viewing azimuth relative to the Sun direction). The antisolar direction (θ_s, 0) is indicated. Each series of ~13 solid dots indicates the different viewing directions corresponding to the target during the same orbit. The six series, from the top to the bottom, are for six different positions of the target through the POLDER swath, from west to east, respectively. Open dots indicate viewing directions within the glitter. Isoscattering angle curves Θ = 100° to 160° in 20° increments are indicated.

measurements are rejected when this radiance is larger than one tenth the molecular radiance at 865 nm, which roughly corresponds to an equivalent aerosol optical thickness of 0.01. Open and solid dots in Figure 1b indicate rejected and selected viewing directions, respectively. Figure 1b shows that the number of viewing directions N, selected in this way, and the resulting range of scattering angle vary largely through the POLDER swath with the best observational conditions for pixels located west off the orbit.

2.2. Principle of the Aerosol Retrieval: Aerosol Models

The aerosol retrieval consists in a two-step approach. In the first step the Ångström exponent and the optical thickness of the aerosols are commonly derived from the radiance measurements in the two aerosol channels. The polarized radiance measurements, whose the reliability is more questionable and has still to be proved, are only used in the second step for the retrieval of the particle refractive index. The procedure for retrieving δ_0 and α is quite similar to that used by *Gordon and Wang* [1997] for SeaWiFS and *Nakajima et al.* [1999] for OCTS. The Ångström exponent of the aerosols (i.e., typically, their mean size) is derived from the mean spectral dependence of the radiance. This yields the aerosol model and hence the aerosol phase function, which permits derivation of the optical thickness from the radiance level. As the radiance measurements are not sensitive enough to the particle refractive index to provide valuable information on m, the retrieval of m is attempted in a second step from the more sensitive polarization measurements.

The algorithm is based on look up tables (LUT) of the directional, spectral, and polarized radiances calculated for different aerosol models with different optical thicknesses. The choice of the models used to build the LUT is a key issue.

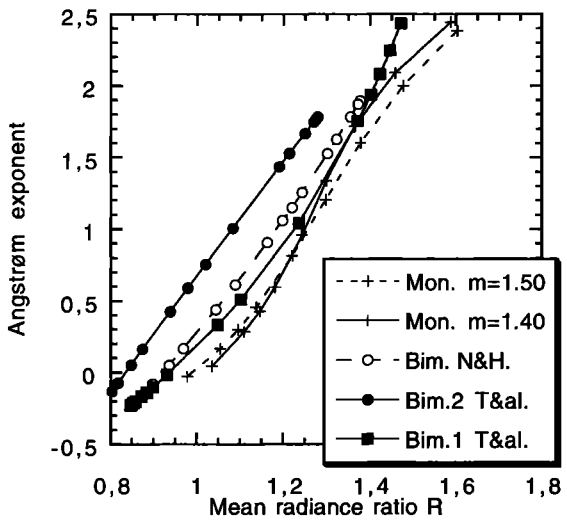

Figure 2. Comparison of the relationship between the mean radiance ratio R (see text) and the Ångström exponent for monomodal and bimodal aerosol models. Monomodal models (Mon.) are for lognormal size distribution with standard deviation σ fixed and modal radius $\bar{r}$ varied; results are shown for real refractive index of the particle $m = 1.40$ and 1.50. Bimodal models (Bim.) are for two lognormal size distributions with standard deviations and modal radii fixed and with the percentages of the two modes varied. Bim. N&H, $\bar{r}_1 = 0.0437$ μm; $\bar{r}_2 = 0.3685$ μm, $\sigma_1 = 0.673$, $\sigma_2 = 0.863$, and $m = 1.50 - 0.005i$ for the two modes [*Higurashi and Nakajima*, 1999]. Bim.1 T&al., $\bar{r}_1 = 0.040$ μm; $\bar{r}_2 = 0.600$ μm, $\sigma_1 = 0.600$, $\sigma_2 = 0.800$, and $m = 1.45 - 0.0035i$ for the two modes Bim.2 T&al, $\bar{r}_1 = 0.080$ μm; $\bar{r}_2 = 1.000$ μm, $\sigma_1 = 0.600$, $\sigma_2 = 0.600$, and $m = 1.50 - 0.0035i$ for the two modes [*Tanré et al.*, 1997]. Here R was calculated by using for $\bar{p}_{\lambda_0}$ the phase function averaged within $100° < \Theta < 160°$.

According to ground-based and airborne observations, many aerosols exhibit multimodal size distributions [e.g., *Shettle and Fenn*, 1979; *Nakajima et al.*, 1986; *Hayasaka et al.*, 1990; *Kaufman et al.*, 1994; *Remer and Kaufman*, 1998]. Such distributions have been used for the data processings of SeaWiFS [*Gordon and Wang*, 1994], OCTS [*Nakajima et al.*, 1999], and the future MODIS [*Tanré et al.*, 1997]. The present algorithm uses simple monomodal lognormal distributions in the form

$$\frac{dN(r)}{d\ln r} = \frac{1}{\sigma\sqrt{2\pi}} \exp\left[-\frac{1}{2}\left(\frac{\ln r - \ln \bar{r}}{\sigma}\right)^2\right]. \quad (1)$$

Nonabsorbing, spherical particles are considered, with three different values of the real refractive index: $m = 1.33$, 1.40, and 1.50. Variation of the refractive index from 670 nm to 865 nm is ignored. The standard deviation of the natural logarithm of the radius is fixed to $\sigma = 0.864$ in equation (1). This gives 0.375 for the standard deviation of the decimal logarithm, which is consistent with the typical values given by *Shettle and Fenn* [1979]. The different models are for values of $\bar{r}$ in equation (1), which yield α ranging from 0.00 to 1.40 (see section 2.3). Linear interpolation between, or linear extrapolation from, these data was shown to provide correct estimate of the radiances for Ångström exponents ranging from −0.5 to 2.0.

The major improvement expected from the present generation of satellite sensors comes from the estimate of the Ångström exponent:

$$\alpha = -\ln(\delta_\lambda/\delta_{\lambda'})/\ln(\lambda/\lambda'), \quad (2)$$

where δ_λ is the aerosol optical thickness, thanks to the multiple near-infrared channels. The aerosol contribution in the TOA radiance is about $\delta_\lambda p_\lambda(\Theta)$, where $p_\lambda(\Theta)$ is the aerosol scattering phase function for scattering angle Θ. Thus measurements at wavelengths λ_0 and λ_1 typically provide $R = \delta_{\lambda_1}\bar{p}_{\lambda_1}/\delta_{\lambda_0}\bar{p}_{\lambda_0}$, where $\bar{p}_\lambda$ stands for some mean value of $p_\lambda(\Theta)$.

Figure 2 shows the relationship between α and R, and Figure 3 shows the relationship between $\bar{p}_{\lambda_0}$ and R for our monomodal models and for bimodal models. The bimodal size distributions are taken from *Higurashi and Nakajima* [1999] (for the analysis of the NOAA AVHRR measurements) and from *Tanré et al.* [1997] (for the analysis of the MODIS measurements over the oceans). For the bimodal models the parameters $\bar{r}$ and σ of the two modes are fixed, and the relative weight of the modes is varied. The aerosol refractive index varies from $1.40–0.0035i$ to $150–0.005i$ depending on the model. For the monomodal models, $\bar{r}$ is varied in equation (1), and results are shown for $m = 1.40$ and 1.50. Here $\bar{p}_\lambda$ is defined as the phase function averaged within $100° < \Theta < 160°$.

Bimodal size distributions are more realistic and versatile than monomodal ones, but Figures 2 and 3 show that an inversion scheme based on monomodal models should give significant results in a first approximation. Moreover, Figure 3 shows that uncertainty in the particle refractive index may be as important as the actual shape of the size distribution and also impacts the estimate of the aerosol optical thickness.

2.3. Detailed Algorithm

The LUT are built for 12 aerosol models: for the three values of m, four values of $\bar{r}$ have been adjusted in equation (1) to yield Ångström exponents $\alpha = 0.00$, 0.30, 0.80, and 1.40. The values for $\bar{r}$ are reported in Table 1. For each aerosol model the TOA radiances and polarized radiances are calculated for four values of the aerosol optical thickness at 865 nm, $\delta_0 = 0.075$, 0.15, 0.30, and 0.60, for a set of observation geometries $(\theta_s, \theta_v, \phi)$, where θ_s is the solar zenith angle, θ_v is the viewing zenith angle, and ϕ is the relative azimuth angle. We assume

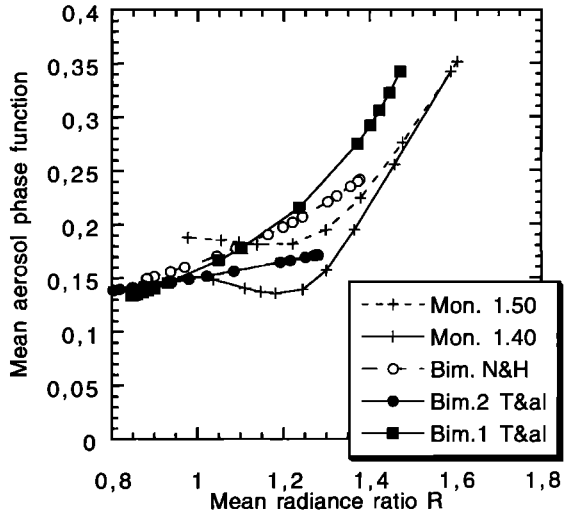

Figure 3. Same as Figure 2 but for the relationship between the mean radiance ratio and the mean aerosol phase function $\bar{p}_{\lambda_0}$; $\lambda_0 = 865$ nm.

linearly polarized light, so that the LUT consist of the Stokes' parameters (L_λ, Q_λ, U_λ).

The computations were made with the successive order of scattering method [*Deuzé et al.*, 1988], taking into account molecular scattering, aerosol scattering, and specular reflection from sea surface. The molecular scattering is estimated according to a standard atmosphere, and the aerosols and molecules are distributed with the altitude according to exponential density profiles with 2 km and 8 km scale height, respectively. In order to test the influence of the vertical structure of the atmosphere, computations were conducted with uniform mixing of aerosols and molecules, i.e., with the same scale height, and the aerosol contributions derived from the two computations by correcting the results for the molecular contribution were compared. For an aerosol optical thickness $\delta_0 = 0.1$, the largest relative discrepancy was 3% in the radiance and 1% in the polarized radiance at wavelength $\lambda = 670$ nm for $\theta_s = \theta_v = 60°$. Because of the small contribution of the molecular scattering at the near-infrared wavelengths considered here, the impact of the vertical structure of the atmosphere is not very large. The specular reflection from the rough ocean surface is derived from the model of *Cox and Munk* [1954] for a fixed wind speed $v = 5$ m/s. Calculations show that the results are nearly insensitive to v for the selected viewing directions. In contrast, the glitter mask is estimated according to the prevailing wind speed provided by the French Meteorological Agency. White caps are assumed to exhibit Lambertian reflectance, ρ_f, with ρ_f derived from *Koepke* [1984] as a function of the prevailing wind speed. The contribution of this Lambertian reflection at the bottom of the atmosphere is added to the radiance of the LUT by taking into account the diffuse and direct transmissions of the atmosphere, as explained by *Tanré et al.* [1990]. The contributions of the water-leaving radiance is neglected. It is certainly negligible at $\lambda = 865$ nm and is very small at $\lambda = 670$ nm, where its reflectance, however, may amount to $\rho_w(670) = 0.001$ according to *Morel* [1983]. All of the results reported in this paper have been obtained with $\rho_w(670) = 0$, which may lead to slight overestimation of the Ångström exponent for aerosol optical thickness lower than 0.10.

In the first step, for each value of m the radiance measurements are compared with the theoretical radiances of the LUT until a best fit is obtained. This provides the parameters α and δ_0 of a "best" monomodal model.

More precisely, we first derive N estimates of α by fitting the two normalized radiances in the N selected viewing directions. For α we retain the average over these estimates. For this value of α we then derive N estimates of the optical thickness from the radiances at 865 nm. We retain for δ_0 the average over these estimates. Finally, the upward radiances and polarized radiances corresponding to retained values of α and δ_0 are derived from the LUT. All of these calculations are processed by using double linear interpolation (extrapolation) between the four α and four δ_0 values of the estimated LUT.

The best models obtained for the three values of m yield nearly similar values of α and slightly different values of δ_0, but the residual discrepancies between the radiance measurements and the theoretical results are nearly the same. Therefore, in a second step the polarization measurements at 865 nm are compared with the theoretical results. The polarization measurements at 670 nm which prove to lead to similar results are not considered. Contrary to the residual discrepancy in the radiances, the residual discrepancy in the polarized radiances differs generally according to m. Interpolation on the refractive index, however, does not seem justified as discussed in section 3.2, and we select the refractive index which leads to minimum residual error in the polarized radiance, with the associated values of α and δ_0. Finally, the impact of the polarization analysis on δ_0 is typically 20%, corresponding to the typical dependence of the aerosol phase function on m.

Table 1. Modal Radius $\bar{r}$ of the Lognormal Aerosol Models Used in the Inversion Scheme

	$m = 1.33$	$m = 1.40$	$m = 1.50$
$\alpha = 0.00$	0.270	0.220	0.180
$\alpha = 0.30$	0.144	0.121	0.100
$\alpha = 0.80$	0.071	0.061	0.051
$\alpha = 1.40$	0.033	0.029	0.025

In units of μm.

Note that another inversion of the POLDER data has been performed through another LUT based on a set of 12 aerosol models of *Shettle and Fenn* [1979]. For each model (i.e., with the value of α fixed) the radiance measurements are compared with the theoretical radiances of the LUT. The best fit is now obtained by adjusting only δ_0, and we just retain this model, which leads to the minimum residual error, with the associated value of α and δ_0. This processing leads to similar order of magnitude of the residual error but, probably because no interpolation is conducted here between the 12 models (hence, between the corresponding values of α), the inverted monomodal model gives quite systematically smaller residual error. Here we will restrict our study to the analysis of the monomodal inversion.

No thresholds were considered in the original algorithm, but preliminary processings showed that the retrieved Ångström exponent was systematically small and slightly negative for very clear pixels (typically, with aerosol optical thickness lower than ~0.05). For such conditions, because the uncertainty in the α retrieval is large, α is no longer calculated, and instead, δ_0 is estimated with $\alpha = 0$. These conditions appear principally over the open ocean, and this value of α is consistent with large maritime aerosols.

3. Results

3.1. Examples of Level 2 POLDER Results

The level 2 POLDER aerosol products, α, δ_0 and m, provided by the CNES POLDER Processing Center are derived according to the previous algorithm. Level 3 products are temporal syntheses (decade or month) of these results at a global scale.

Validation of the α and δ_0 retrievals has been examined by *Goloub et al.* [1999] from comparison with correlative measurements provided by Aerosol Robotic Network (AERONET) [*Holben et al.*, 1998]. The retrieved aerosol optical thickness proves to be in agreement with ground-based measurements within ~0.05 rms for $\delta_0 < 0.8$. The Ångström exponent derived from POLDER is systematically slightly underestimated but is well correlated with the estimate of α derived from AERONET using the same wavelengths as POLDER. No validation of the aerosol refractive index as a self-standing POLDER parameter has been considered. Typical examples of level 3 products of δ_0 and α have been published [*Deuzé et al.*, 1999]. The main geographical and seasonal features observed in these global maps are consistent with the properties of the aerosols derived previously from the AVHRR data with respect to their mean content [*Stowe et al.*,

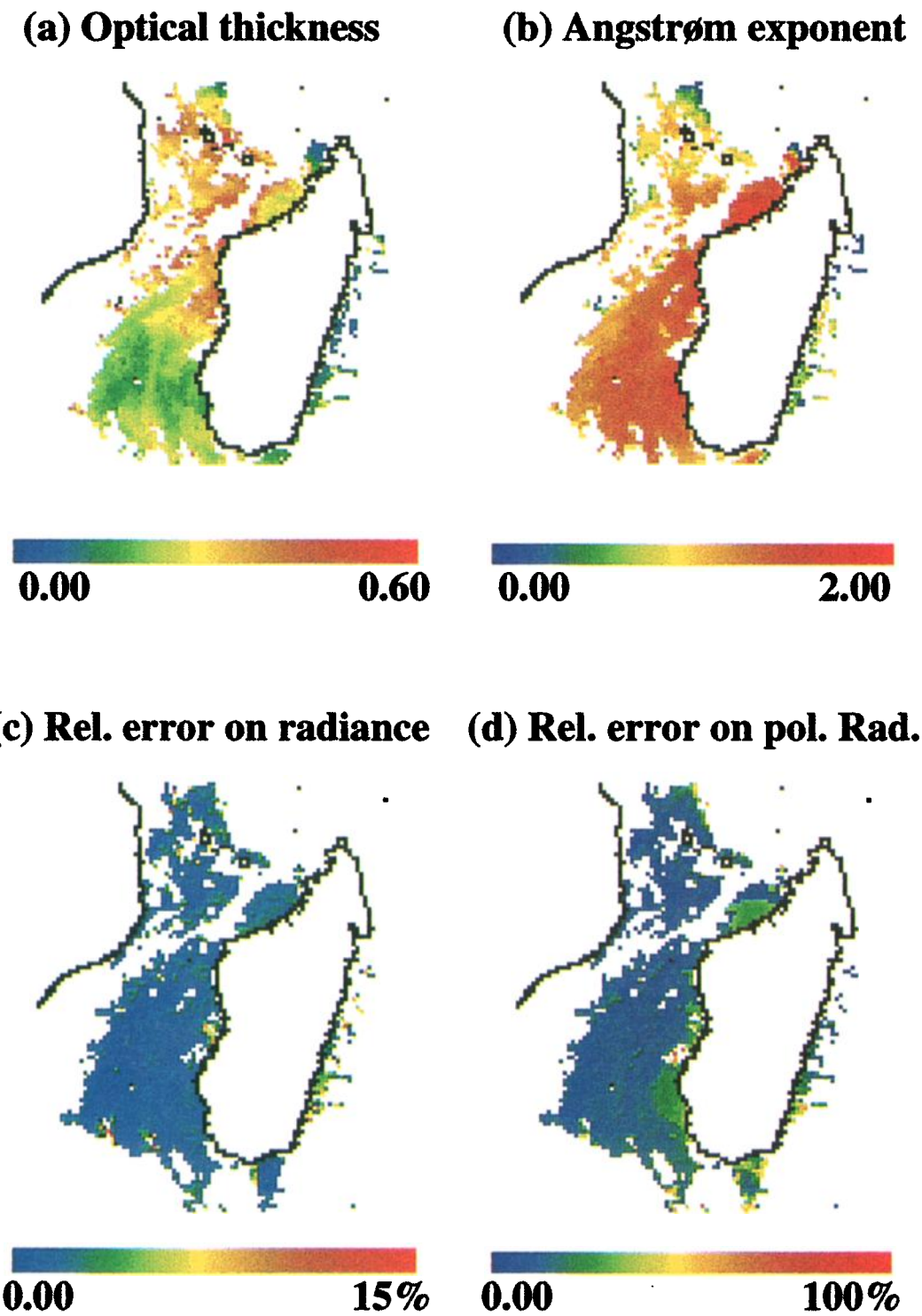

Plate 1. Observed area between Madagascar and South Africa from POLDER orbit 3248, November 20, 1996. Land and cloudy pixels are in white. For each cloud-free ocean pixel, (a) the derived aerosol optical thickness δ_0, (b) the Ångström exponent α, (c) the residual relative error in the radiance retrieval $\bar{\Delta}L/\bar{L}$, and (d) the residual relative error in the polarized radiance retrieval, $\bar{\Delta}L^p_\lambda/\bar{L}^p_\lambda$ are shown. The color code is indicated. Values increase from blue to red.

1992; *Husar et al.*, 1997] or size [*Higurashi and Nakajima*, 1999]. Here we examine the consistency of the inversion scheme by using the multidirectional and polarized capabilities of POLDER to estimate the accuracy of the data fitting depending on the kind of aerosol that we are observing.

The POLDER level 2 aerosol products are detailed here for four aerosol patterns over areas a few hundred kilometer wide, with aerosol loading large enough to make clear the aerosol signature in the measurements. The scenes have been selected westward of the POLDER swath in order to test the consistency of the results over an extended range of scattering angles (see Figure 1b). For eastward pixels at midlatitudes the few

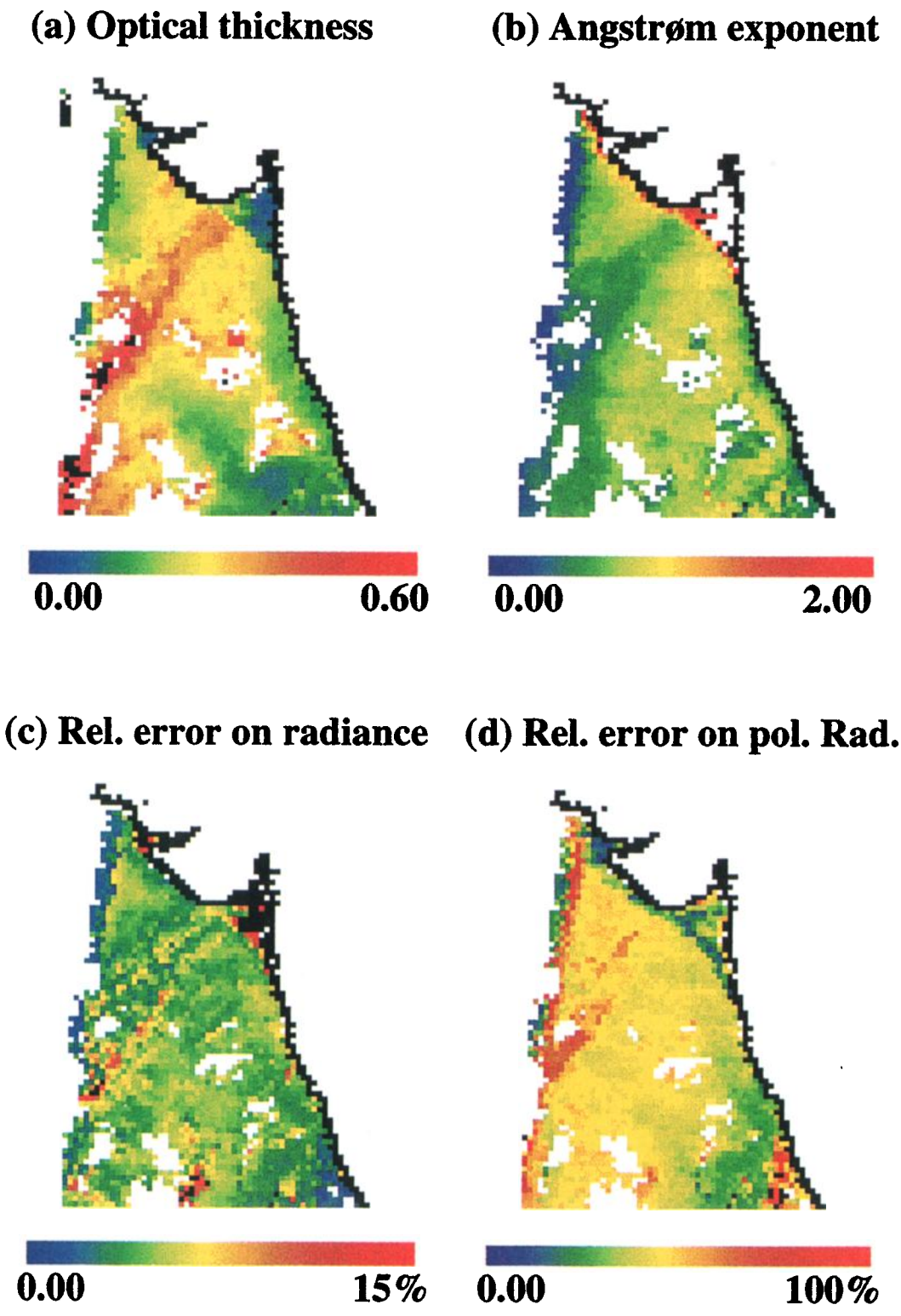

Plate 2. Same as Plate 1 but for an area west off India from POLDER orbit 3447, December 4, 1996.

viewing directions no longer exhibit significant directional effect and merge practically into three data sets (radiances at 670 and 865 nm and polarized radiance at 865 nm) that may be fitted with the free parameters of the algorithm. The four cases are representative of the performances, from the best to the worst, obtained by the present inversion scheme according to the aerosol type.

Plate 1 shows an area near Madagascar, on November 20, 1996 (orbit 3248); Plate 2 shows an area over the Arabian Sea, west off the Indian continent, on December 4, 1996 (orbit

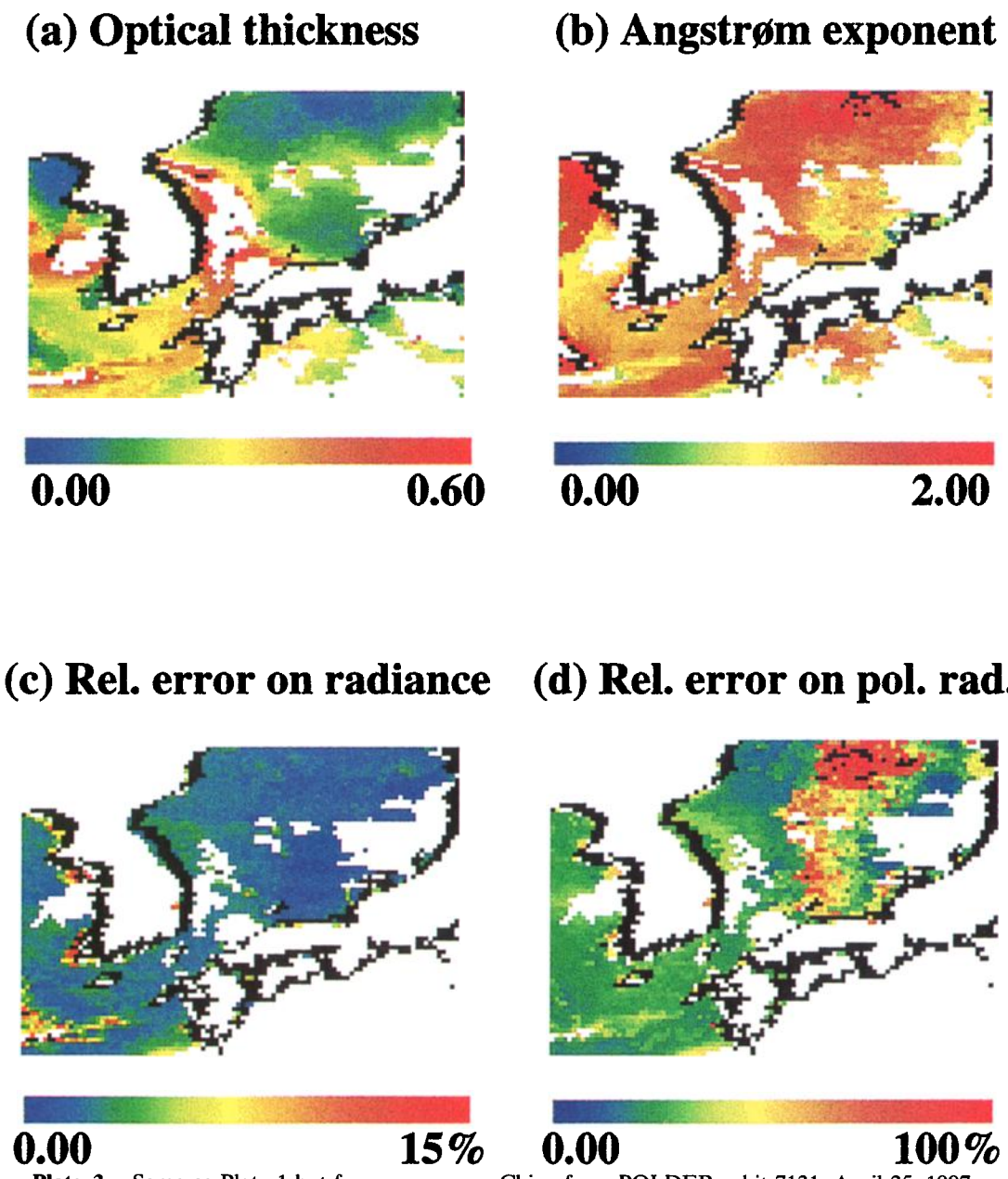

Plate 3. Same as Plate 1 but for an area near China from POLDER orbit 7131, April 25, 1997.

3447); Plate 3 shows an area near China, on April 25, 1997 (orbit 7131), and Plate 4 shows an area over the Atlantic Ocean, west off the African coast, on March 1, 1997 (orbit 5522). Plates 1–4 first display images of the δ_0 and α retrievals. The large value of the mean Ångström exponent (~1.40) in Plate 1 is consistent with biomass burning aerosols between Madagascar and South Africa at the end of the biomass burning period. The moderate value of α (0.60) in Plate 2 corresponds probably to pollution aerosols coming from the Indian continent, according to the prevailing mean wind direction. Large Ångström exponents are observed again over the Chinese area (1.40). Finally, the small Ångström exponent (0.30) in Plate 4 is consistent with desertic particles from the Sahara. The refractive index retrievals are not presented. The retrieved value is nearly the same, $m = 1.33$, all over the areas of Plates 1, 2, and 4 and ranges from 1.33 to 1.40 over the area of Plate 3.

3.2. Radiance Analysis

Let us first consider the consistency between the radiance measurements and the theoretical results. For one single pixel of Plates 1 and 2 the measured radiances and the best theoretical results for each value of m have been reported as a function of the scattering angle in Figures 4 and 5, respectively. For comparison, the radiances calculated without aerosols in the atmosphere (molecular terms) have been also reported. Note that different viewing directions may lead to the same scattering angle, while the air mass differs, as for the Madagascar case. The three theoretical results are very close in Figures 4 and 5, which shows that it is difficult to derive information about the aerosol refractive index from directional and spectral radiance measurements. As outlined in section 2.3 the retrieved Ångström exponent (1.40 and 0.39 in Figures 4 and 5, respectively) is nearly independent on the assumed refractive

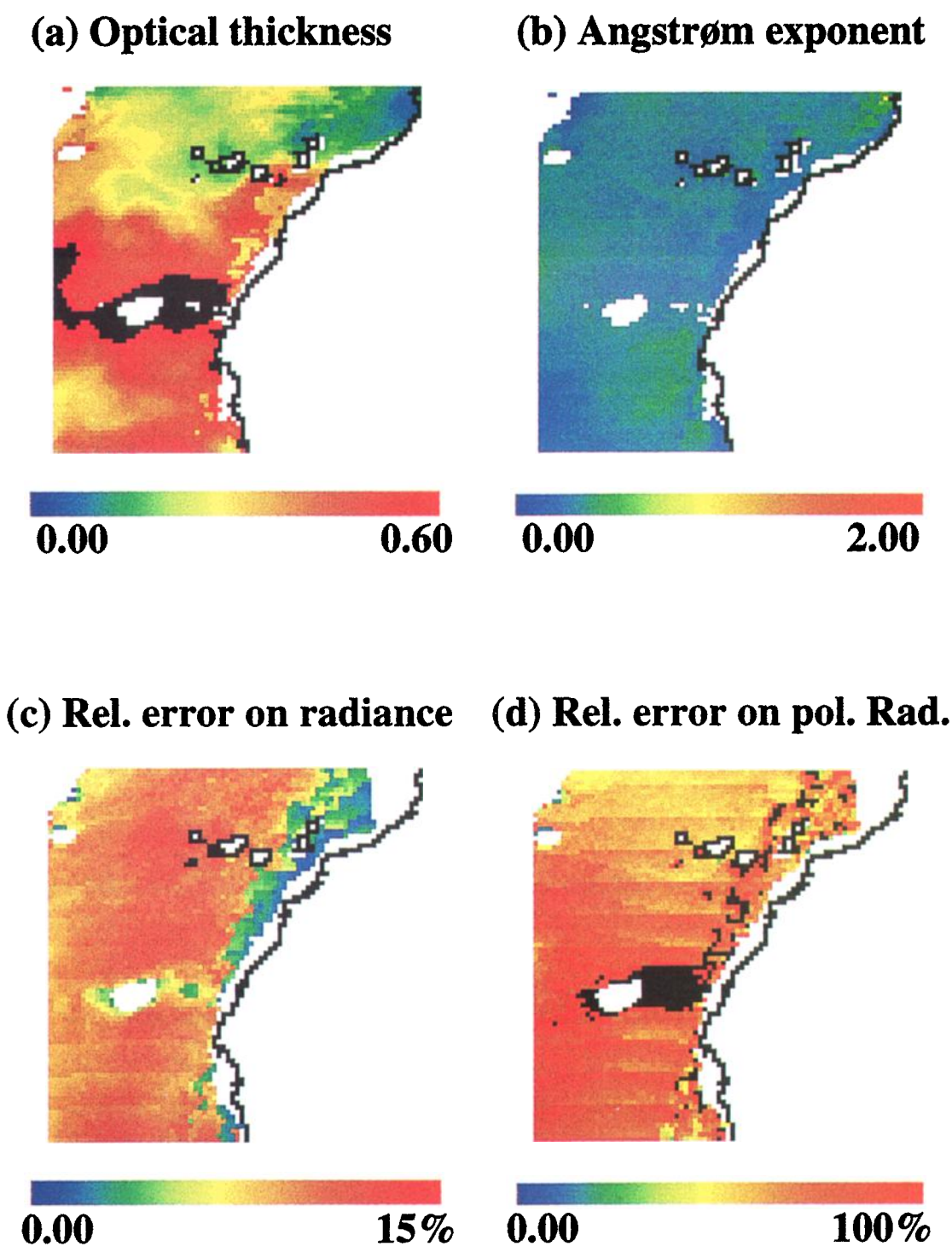

Plate 4. Same as Plate 1 but for an area west off Africa from POLDER orbit 5522, March 1, 1997.

index and the retrieved optical thickness (0.33 and 0.51 in Figures 4 and 5, respectively) is typically 20% lower (larger) for $m = 1.50$ ($m = 1.33$) than for $m = 1.40$. In any case, Figures 4 and 5 show that the directional feature predicted by the aerosol model which fits the mean bispectral radiances is roughly consistent with the measurements. However, while the results are very good for the Madagascar case, some discrepancies appear in the Indian one.

To extend the comparison to the whole scenes, Plates 1c, 2c, 3c, and 4c display the relative residual error in the radiance for each image pixel, i.e., $\bar{\Delta}L/\bar{L}$, where $\bar{L}$ is the radiance averaged over the $2N$ measurements (i.e., N is selected viewing directions in the two aerosol channels), i.e.,

$$\bar{L} = \frac{1}{2N} \sum_{i=1}^{N} \sum_{j=0}^{1} L_{\lambda_j}^{m}(\Theta_i), \tag{3}$$

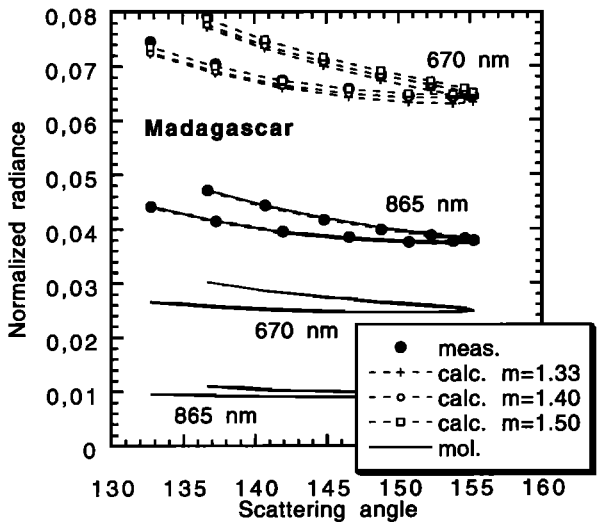

Figure 4. Normalized radiances as a function of the scattering angle resulting from the viewing geometry for a pixel near Madagascar (from Plate 1). The POLDER measurements in the 670- and 865-nm channels are compared with the theoretical results for the three best models for the three values of the aerosol refractive index (1.33, 1.40, and 1.50). Retrieval: Ångström exponent of 1.40; aerosol optical thickness 0.33 at 865 nm for $m = 1.33$. For comparison, the results for an aerosol-free atmosphere (mol.) are indicated.

and $\bar{\Delta}L$ the residual quadratic error

$$\bar{\Delta}L = \sqrt{\frac{1}{2N}\sum_{i=1}^{N}\sum_{j=0}^{1}[L_{\lambda_j}^m(\Theta_i) - L_{\lambda_j}^c(\Theta_i)]^2}; \qquad (4)$$

L_λ^m and L_λ^c stand for the measurements and the computations, respectively. $\bar{\Delta}L/\bar{L}$ has been calculated for the three values of m, and the smallest value is reported.

The results of Plates 1–4 are representative of the global results. The directional properties predicted by our monomodal models are in excellent agreement with the measurements for the case of small aerosols with large Ångström exponents, as shown here in Plates 1 and 3. However, as larger particles are present, although the retrieved values of δ_0 and α are still consistent with the ground-based measurements, increasing discrepancies are observed in the directional features: the residual error in the radiance data fitting increases from a few percents as in Plates 1 and 3, up to 5% as in Plate 2 or 10–15% as in Plate 4.

3.3. Polarization Analysis

In the second step the Stokes' parameters derived from the LUT for the best model associated to each value of m are compared with the measurements. Instead of the Stokes' parameters (Q_λ, U_λ), let us consider the equivalent and more physical parameters (L_λ^p, ψ_λ), where L_λ^p is the normalized polarized radiance ($L_\lambda^p = \sqrt{Q_\lambda^2 + U_\lambda^2}$), and ψ_λ is the angle between the polarization direction and the normal to the scattering plane (formed by the solar and observation directions).

Let us first consider the Madagascar pixel. The measured polarized radiance, L_λ^p, and the three best theoretical results have been reported in Figure 6a as a function of the scattering angle. For comparison, the polarized radiance calculated without aerosols in the atmosphere have also been reported. Figure 6b shows the same comparison for the polarization angle ψ_λ. Note that single scattering within the atmosphere should give a polarized vibration either perpendicular ($\psi_\lambda = 0°$) or parallel ($\psi_\lambda = 90°$) to the scattering plane. Figure 6b, however, shows that multiple scattering and scattering of the polarized light reflected from the sea surface may produce large departures of ψ_λ from 0° or 90°, specially in backscattering directions.

The large differences between the three theoretical results in Figures 6a and 6b illustrate the sensitivity of polarization to the particle refractive index [*Hansen and Travis*, 1974]. On the other hand, both the amount of polarized light and the polarization direction here are nearly consistent with the theoretical results for $m = 1.33$. The results are summarized in Figure 6c, which shows the residual error in the polarized light as a function of the scattering angle, i.e.,

$$\Delta L_\lambda^p/L_\lambda^p = \sqrt{(Q_\lambda^m - Q_\lambda^c)^2 + (U_\lambda^m - U_\lambda^c)^2}/L_\lambda^p \qquad (5)$$

for the three values of m. Note that the lowest residual error for $m = 1.33$, about 15% (i.e., roughly 0.0015 in terms of normalized polarized radiance), is larger than the NEDL_λ^p, 0.0004, which suggests that the present retrieval could be improved by using more flexible aerosol models in the algorithm. To extend to the whole scene an estimate of the error, Plate 1d displays the mean residual error in the polarized light

$$\frac{\bar{\Delta}L_\lambda^p}{\bar{L}_\lambda^p} = \frac{\left(\frac{1}{N}\sum_{i=1}^{N}[Q_{\lambda_0}^m(\Theta_i) - Q_{\lambda_0}^c(\Theta_i)]^2 + [U_{\lambda_0}^m(\Theta_i) - U_{\lambda_0}^c(\Theta_i)]^2\right)^{1/2}}{\frac{1}{N}\sum_{i=1}^{N}\sqrt{Q_{\lambda_0}^m(\Theta_i)^2 + U_{\lambda_0}^m(\Theta_i)^2}} \qquad (6)$$

obtained for each image pixel with the best value for m (here $m = 1.33$ for most pixels of the scene). The results are correct all over

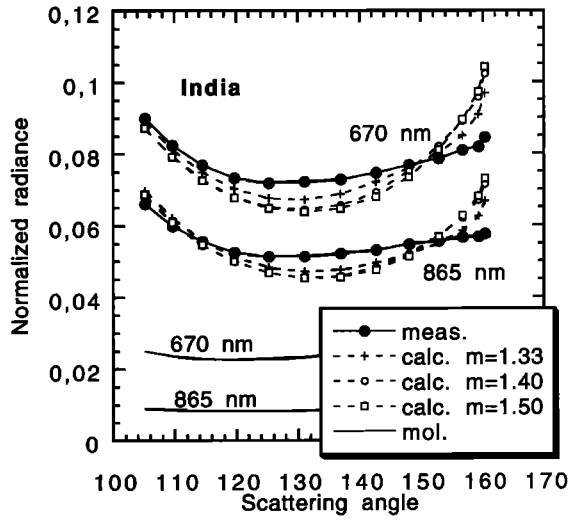

Figure 5. Same as Figure 4 but for a pixel near Indian continent (from Plate 2). Retrieval: Ångström exponent of 0.39; aerosol optical thickness 0.51 at 865 nm for $m = 1.33$.

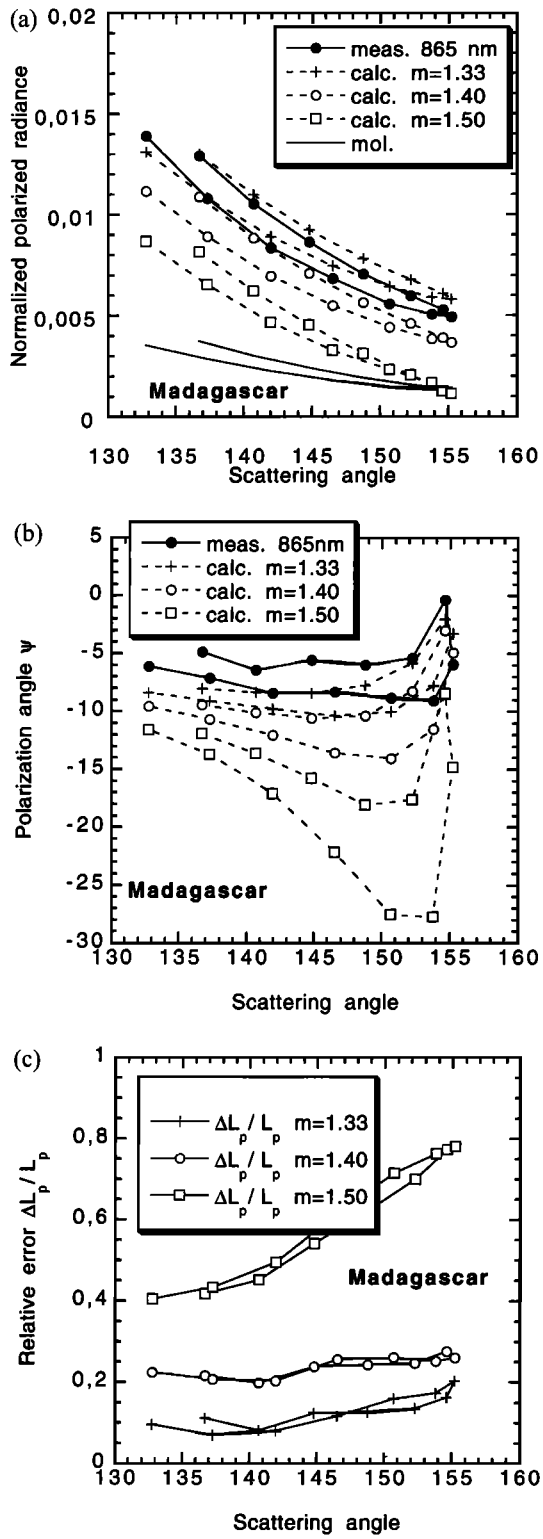

Figure 6. (a) Madagascar pixel of Figure 4. Normalized polarized radiance ($\sqrt{Q_\lambda^2 + U_\lambda^2}$) as a function of the scattering angle. The POLDER measurements in the 865-nm channel are compared with the theoretical results for the three best models for the three values of the aerosol refractive index (1.33, 1.40, and 1.50). For comparison, the results for an aerosol-free atmosphere (mol.) are indicated. (b) Angle ψ_λ between the polarization direction and the normal to the scattering plane. (c) Residual relative error in the retrieved polarized radiance, $\overline{\Delta L}_\lambda^p / \overline{L}_\lambda^p$, according to the assumed particle refractive index (1.33, 1.40, and 1.50), as a function of the scattering angle Θ.

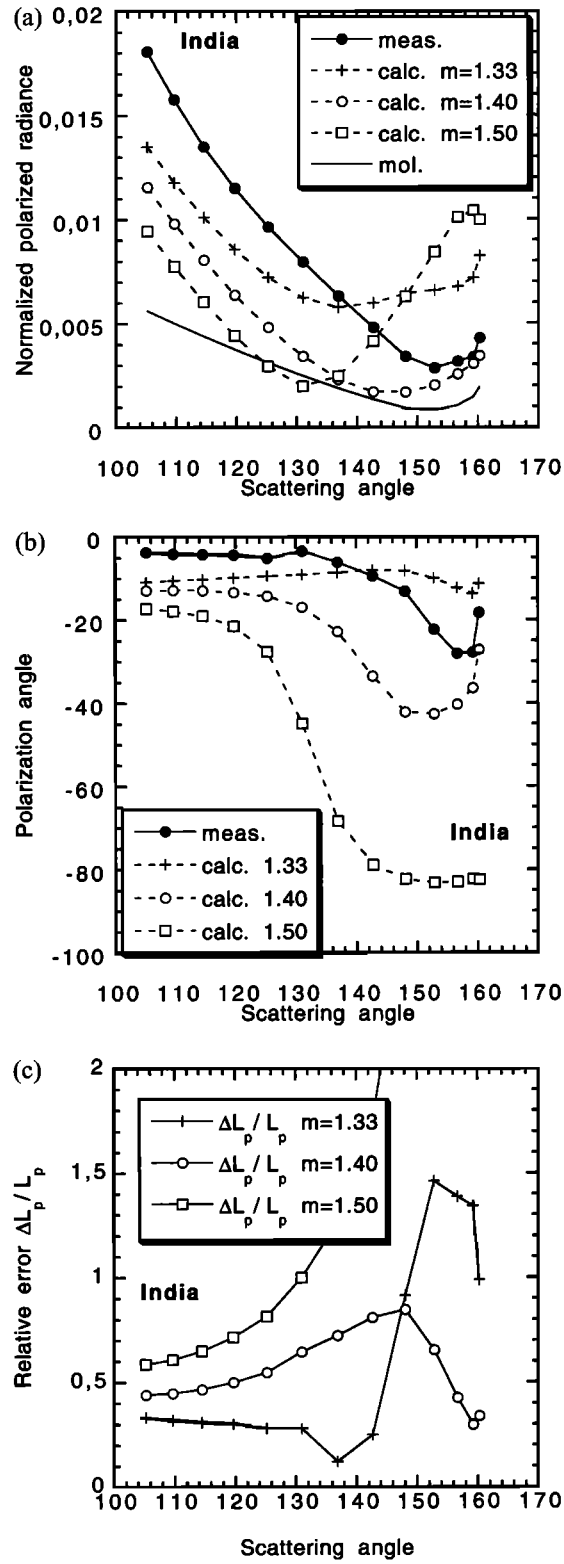

Figure 7. Same as Figure 6, but for Indian pixel of Figure 5.

the area. Plates 3c and 3d show that similar conclusions are obtained for the aerosols observed near China which correspond to small aerosols as the aerosol type observed near Madagascar.

On the contrary, the matching of the polarization data may be much more questionable or meaningless as illustrated by Figures 7a–7c for the pixel of the Indian scene of Plate 2. The

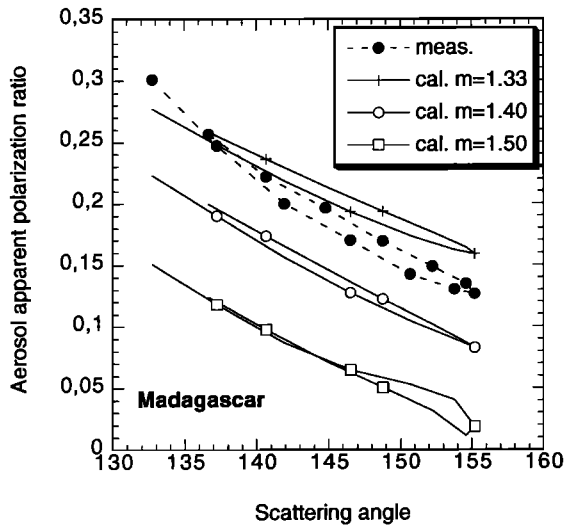

Figure 8. Madagascar pixel of Figure 4. Aerosol apparent polarization ratio (see text) as a function of the scattering angle. The estimate P_λ^m derived from the POLDER measurements in the 865-nm channel is compared with the theoretical result P_λ^c for the best model obtained for the each value of the aerosol refractive index (1.33, 1.40, and 1.50).

agreement here is rather poor for the three values of m. The results are even worse for the African scene as indicated by the large value of $\bar{\Delta}L_\lambda^p/\bar{L}_\lambda^p$ in Plate 4. Clearly, in such cases the analysis of the polarized light fails, and the retrieved refractive index is meaningless within the present inversion scheme when larger aerosols are observed.

4. Discussion

4.1. Behavior of the Residual Errors

As shown in section 3.3, the data fitting achieved with the present algorithm leads to increasing errors in the retrieved polarization and directional radiance when the aerosol dimension increases. Concerning the directional radiance, comparison between observations and calculations clearly shows that our aerosol models tend to overestimate the dissymmetry of the phase function of large aerosols, as seen in Figure 5. On the other hand, comparison between observations and calculations of L_λ^p and ψ_λ gives no straightforward indication about the defect of the modeling with respect to the polarization.

To clarify, let us discard ψ_λ and only consider the polarization ratio, L_λ^p/L_λ, which should no longer depend on the aerosol optical thickness and should be controlled by their single scattering properties. More precisely, let us correct the measurements for the molecular contribution and consider the apparent polarization ratio of the light scattered by the aerosols,

$$P_\lambda^m = \frac{\sqrt{(Q_\lambda^m - Q_\lambda^{\mathrm{mol}})^2 + (U_\lambda^m - U_\lambda^{\mathrm{mol}})^2}}{L_\lambda^m - L_\lambda^{\mathrm{mol}}} \qquad (7)$$

where L_λ^{mol}, Q_λ^{mol}, U_λ^{mol} stand for computations without aerosols within the atmosphere. Although the multiple scattering and surface reflection effects are not corrected for in equation (7), comparison between P_λ^m and theoretical calculations, say P_λ^c (with L_λ^c, Q_λ^c, U_λ^c in place of L_λ^m, Q_λ^m, U_λ^m in equation (7)), should help us to understand the origin of the discrepancies.

Figures 8 and 9 compare P_λ^m and P_λ^c for the Madagascar and Indian cases, respectively. Figure 8 shows the same agreement as seen in Figure 6, but Figure 9 clearly displays the origin of the discrepancy for the case of the Indian aerosol. In Figure 9 the measurements exhibit the typical signature of submicrometric particles whose the polarization increases regularly when the scattering angle decreases, while the theoretical results exhibit principally the rainbow-like feature of large spherical particles within the range $140° < \Theta < 180°$. In these directions, single scattering gives a polarized vibration parallel to the scattering plane (i.e., $\psi_\lambda = 90°$) [*Hansen and Hovenier*, 1974], which results in large polarized reflectances with ψ_{λ_0} far from 0° as illustrated in Figures 7a, 7b, and 9. Concerning the polarization, the main shortcoming of our models therefore consists in an underestimation of the polarized light at side-scattering angles, within the range $80° < \Theta < 120°$.

To assess the validity of this comparison, the single scattering polarization ratios corresponding to the theoretical models used in Figure 9 have been reported in Figure 10. Comparison of Figures 9 and 10 confirms that P_λ^c roughly mirrors the single scattering properties of the particles. Note also that if we proceed inversely and search directly for aerosol models consistent with the large values of P_λ^m in Figure 9, the retrieved models yield radiance ratios, L_{670}/L_{865}, about 7% larger than the measured ratios. According to *Hagolle et al.* [1999] the accuracy of the interband calibration between the two aerosol channels is 2%. Therefore the 7% departure is not due to measurement errors but must be attributed to the aerosol models.

These trends are persistent features throughout the POLDER data set. The 8 months of POLDER data over various areas all over the oceans have been processed, and Plates 5 and 6 show the resulting relationships between the retrieved Ångström exponent and the residual errors $\bar{\Delta}L_\lambda^p/\bar{L}_\lambda^p$ and $\bar{\Delta}L/\bar{L}$, respectively. In Plates 5 and 6 the results are for ground pixels with $\delta_0 > 0.20$ and with Θ ranging over an interval larger than 30°, which allows valuable control of the data fitting accuracy. The results are shown in the form of normalized frequency of occurrence.

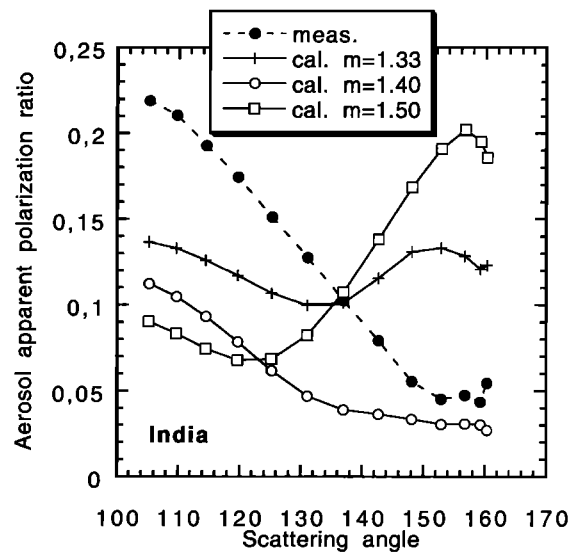

Figure 9. Same as Figure 8, but for Indian pixel shown in Figure 5.

In the presence of small aerosols the theoretical results are consistent with the observations, with $\bar{\Delta}L^p_\lambda/\bar{L}^p_\lambda \approx 0.10$ to 0.30 and $\bar{\Delta}L/\bar{L} \approx 0.01$ to 0.03 for α larger than about 1.0. In the presence of larger particles, the polarization analysis (Plate 5) tends to fail progressively, with $\bar{\Delta}L^p_\lambda/\bar{L}^p_\lambda$ as large as 80% to 100% for large desertic particles ($\alpha < 0.20$). Plate 6 shows that increasing errors in the directional radiances are observed correlatively.

4.2. Analysis of the Polarization Defect

First, let us consider the underestimation of polarized light for side-scattering angles by using our models. As polarization is very sensitive to the properties of the particles, many explanations for the failure of the polarization analysis may be suggested, including nonsphericity of the particles which may entail large departures from Mie theory calculations. However, departure from sphericity tends generally to lower the polarized light scattered by the particles [*Cai and Liou*, 1982; *De Haan*, 1987; *Brogniez*, 1992; *Masuda and Takashima*, 1992; *Mishchenko and Travis*, 1994a, b]. Therefore it may be expected that our spherical models should lead to an overestimation of the polarized light in the presence of nonspherical particles. Moreover, polarization at side-scattering angles is mainly generated by very small particles [*Hansen and Travis*, 1974] whose scattering properties are not too sensitive to shape effects [*Mishchenko and Travis*, 1994a, b]. Hence, the defect of the present modeling very likely consists of an underestimation of the submicrometric particles in the assumed aerosol size distribution, which seems indicative of bimodality of the aerosols.

Let us consider bimodal aerosol size distributions drawn from the dynamic models of *Remer and Kaufman* [1998] and *Kaufman et al.* [1994] and consisting of small (S) and coarse (C) modes of particles, both of the modes being in the form of a lognormal function according to equation (1). In what follows, the calculations are for a coarse mode with modal radius

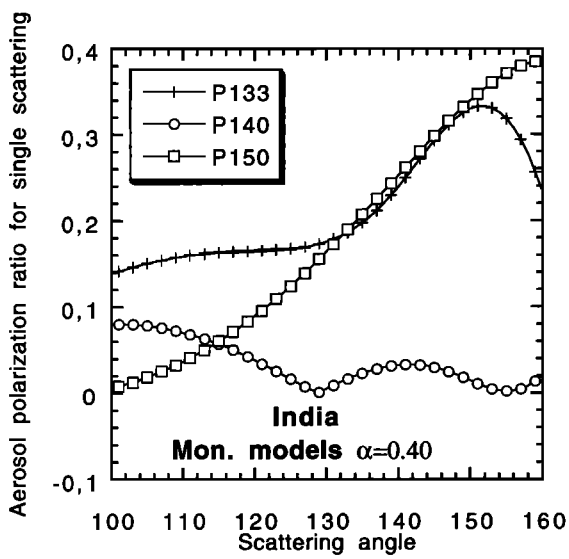

Figure 10. For the Indian pixel of Figures 5, 7, and 9, the polarization ratio for single scattering, P_λ, for the three best models (m = 1.33, 1.40, 1.50) is reported as a function of the scattering angle. Comparison of P_λ with P^c_λ, in Figure 9, confirms that the apparent polarization ratio reflects the aerosol single scattering features.

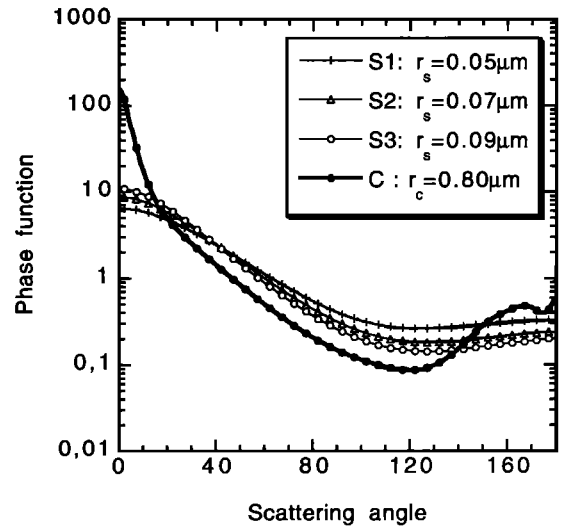

Figure 11. Phase functions at wavelength λ_0 = 865 nm for the coarse mode (C) and three different small modes (S) of particles, which are used for simulating bimodal aerosol size distributions. The particle refractive index is m = 1.40. Note that the dissymmetry of the phase function of the coarse mode is not changed significantly by changing m or r_C.

$\bar{r}_C$ = 0.80 μm and a small mode whose the modal radius $\bar{r}_S$ may range from 0.05 μm to 0.10 μm, with identical standard deviations $\sigma_C = \sigma_S$ = 0.60 for the two modes. All of the calculations are for spherical particles with real refractive index m = 1.40. Figures 11 and 12 show the typical phase functions and polarized phase functions of these small and coarse modes for wavelength λ_0 = 865 nm. Calculations (not presented here) show that changing m or changing largely $\bar{r}_C$ does not change the main following statements.

Figure 13 compares the polarization ratios for single scattering computed for the monomodal model $\bar{r}$ = 0.04 μm, σ = 0.8635, and for different bimodal models which were obtained by mixing the previous coarse mode with different small modes, the contributions of the two modes being adjusted to yield the same radiance ratio R as that yielded by the monomodal model (here R = 1.27). The polarization ratio at side-scattering angles is systematically larger for all of these "equivalent" bimodal models than it is for the monomodal model. This is rational. Let us start with very small particles. To adjust R with an assumed monomodal distribution, the size distribution is translated toward larger dimensions, which entails vanishing contribution of the small polarizing particles, while with an assumed bimodal distribution, R is changed by increasing the weight of the coarse mode which preserves the polarized light from the small aerosols.

The previous trend is systematic. The polarized phase function for λ_0 and for Θ = 110° was calculated for various monomodal models (say q_m). In each case, different bimodal models obtained as in Figure 13 were adjusted to yield the same radiance ratio R as yielded by the monomodal model, and the polarized phase functions for λ_0 and Θ = 110° of these equivalent models were calculated (say q_b). Figure 14 shows the resulting relationship between the Ångström exponent of the monomodal model and the departure between its polarization ratio and that of its equivalent bimodal models:

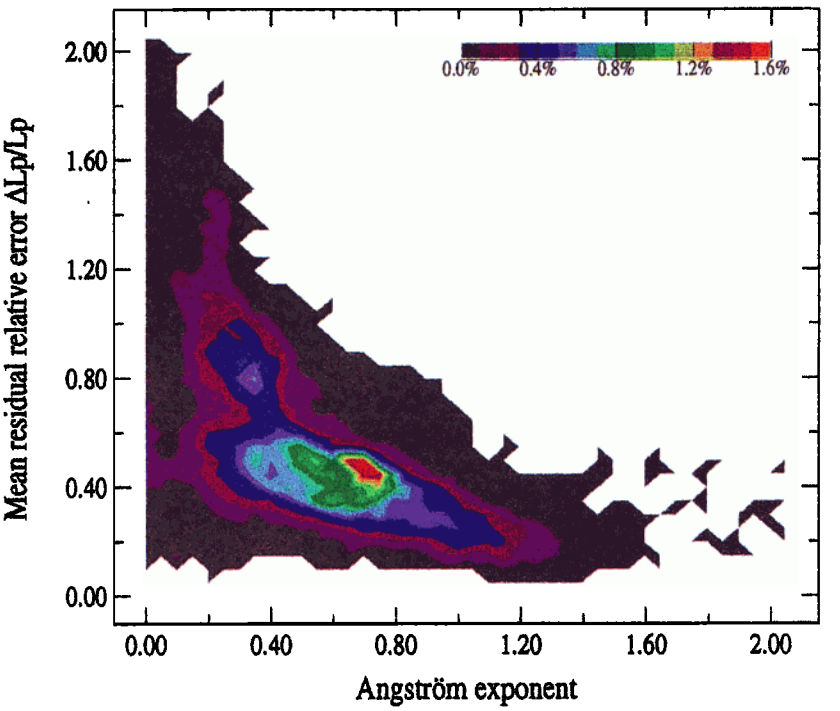

Plate 5. For 8 months of POLDER aerosol observations over different areas all over the oceans. The residual error in the polarized radiance, $\bar{\Delta}L^p_\lambda/\bar{L}^p_\lambda$, is reported as a function of the retrieved Ångström exponent for each pixel. Color indicates the frequency of occurrence of the result (arbitrary units). The results are for ground pixels with $\delta_0 > 0.20$ and $\Delta\Theta > 30°$, which provides a significant test of the model consistency. The retrieval is rather successful for small particles ($\alpha > 1.0$), but the accuracy decreases systematically for larger particles.

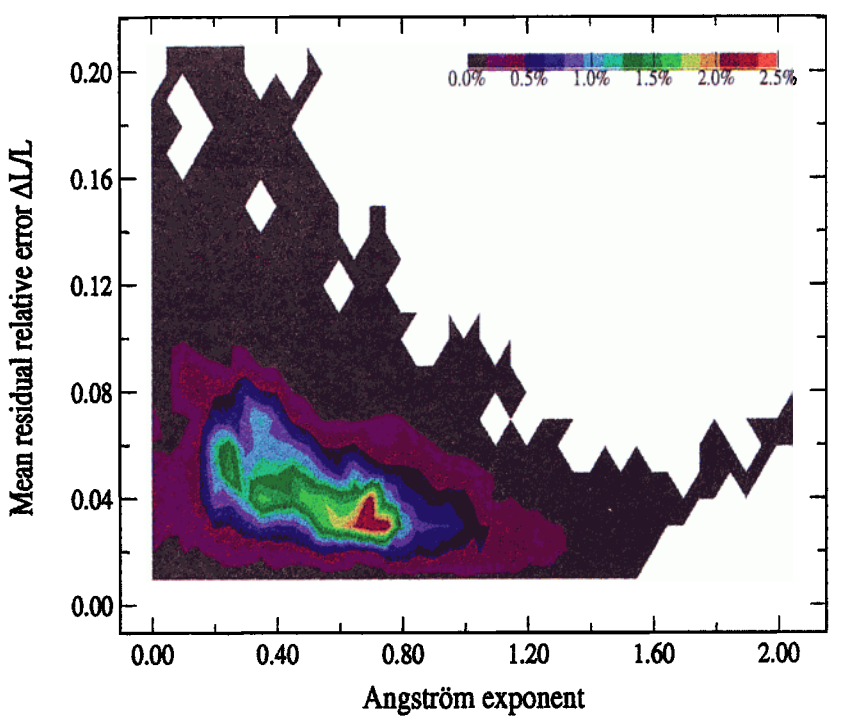

Plate 6. Same as Plate 5 but for the residual error in the total radiance, $\bar{\Delta}L/\bar{L}$. In the presence of large aerosols the present aerosol modeling exhibits inadequacy both regarding the phase function and polarized phase function of the particles.

$$\frac{\Delta q}{q} = \frac{q_b - q_m}{q_b}. \quad (8)$$

The order of magnitude of $\Delta q/q$ and its behavior as a function of α in Figure 13 are consistent with the residual error $\bar{\Delta}L^p_\lambda/\bar{L}^p_\lambda$ in Plate 5, which confirms that the observed failure in the polarization retrieval is likely indicative of bimodality of the aerosols, with the parameters of the bimodal models in rough agreement with those of the dynamic models of *Remer and Kaufman* [1998].

4.3. Analysis of the Directional Radiance Defect

Then let us look at the discrepancy in the directional radiances. It may be thought that bimodality of the aerosol size distribution should also explain this systematic defect by way of the small particles whose the phase function is nearly isotropic in backscattering directions, as seen in Figure 11. Figure 15 compares the phase functions of the monomodal model and equivalent bimodal models used in Figure 13. Some choices for $\bar{r}_S$ in Figure 15 lead to a phase function of the bimodal model a little bit more isotropic than that of the monomodal model, but this effect is not systematic and, especially, as the mean size of the particles increases the difference between the phase functions of a monomodal model and of an equivalent bimodal model decreases.

Let us estimate the dissymmetry of a phase function by $D = \bar{p}(160°)/\bar{p}(110°)$, where $\bar{p}(110°)$ and $\bar{p}(160°)$ stand for the average value of $p(\Theta)$ over the ranges $100° < \Theta < 120°$ and $150° < \Theta < 170°$, respectively. For the same cases as in Figure 14, Figure 16 shows the relationship between the Ångström exponent of the monomodal model and the departure between its dissymmetry and that of its equivalent bimodal models:

$$\frac{\Delta D}{D} = \frac{D_m - D_b}{D_b}, \quad (9)$$

where D_m and D_b are the dissymmetries of the monomodal and equivalent bimodal models, respectively. As α decreases, the influence of the small mode decreases and $\Delta D/D$ vanishes since the aerosol phase function tends toward that of large spherical particles whether a monomodal or a bimodal model is assumed. The resulting behavior of $\Delta D/D$ as a function of α in Figure 16, therefore, is nearly the opposite of that of $\bar{\Delta}L/\bar{L}$ in Plate 6. Thus bimodality of the size distribution of spherical particles cannot explain all of the trends of the results.

Therefore we are faced with polarization measurements at

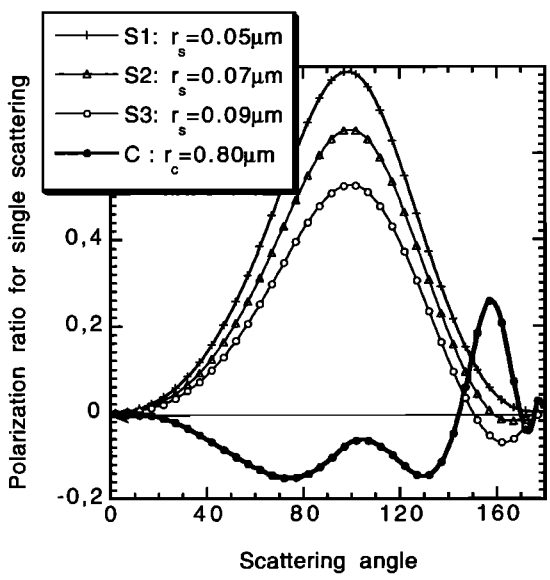

Figure 12. Same as Figure 11 but for the polarized phase functions of the coarse and small modes.

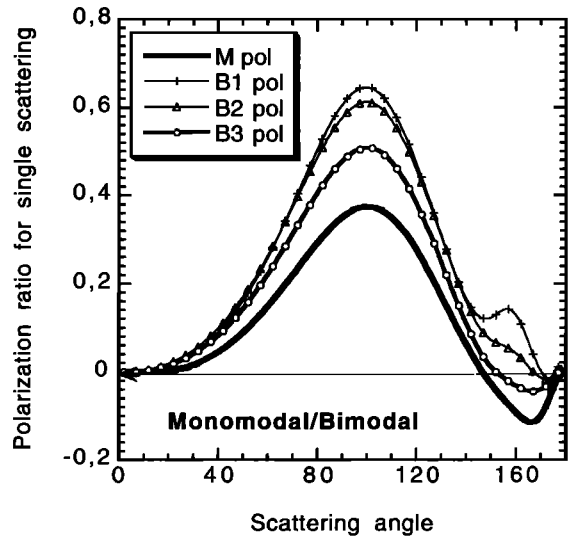

Figure 13. Polarized phase functions at wavelength $\lambda_0 = 865$ nm for spherical particles with a monomodal size distribution (M, $\bar{r} = 0.04$ µm, $\sigma = 0.8635$; $m = 1.40$; $\alpha = 1.15$) and for spherical particles with three different "equivalent" bimodal size distributions (B1, $\bar{r}_S = 0.05$ µm; B2, $\bar{r}_S = 0.07$ µm; B3, $\bar{r}_S = 0.09$ µm; and $\bar{r}_C = 0.80$ µm, $\sigma_C = \sigma_S = 0.60$ and $m = 1.40$). For each bimodal model the contributions of the two modes have been adjusted to yield the same radiance ratio $R = \delta_{\lambda_1}\bar{p}_{\lambda_1}/\delta_{\lambda_0}\bar{p}_{\lambda_0}$ as that yielded by the monomodal model ($R = 1.27$).

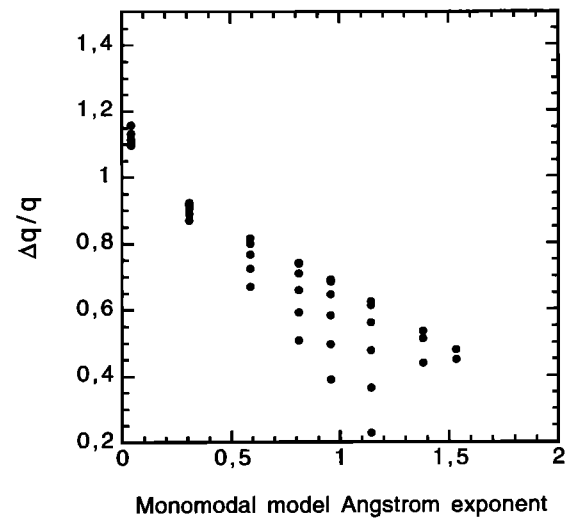

Figure 14. Expected relationship between the Ångström exponent α of the retrieved monomodal model and the discrepancy $\Delta q/q = (q_b - q_m)/q_b$ in the polarized light retrieval near scattering angle $\Theta = 110°$ in the presence of aerosols with bimodal size distribution. For different values of α, q_m and q_b are the polarized phase functions $q_{\lambda_0}(110°)$ for monomodal and equivalent bimodal models which yield the same radiance ratio R.

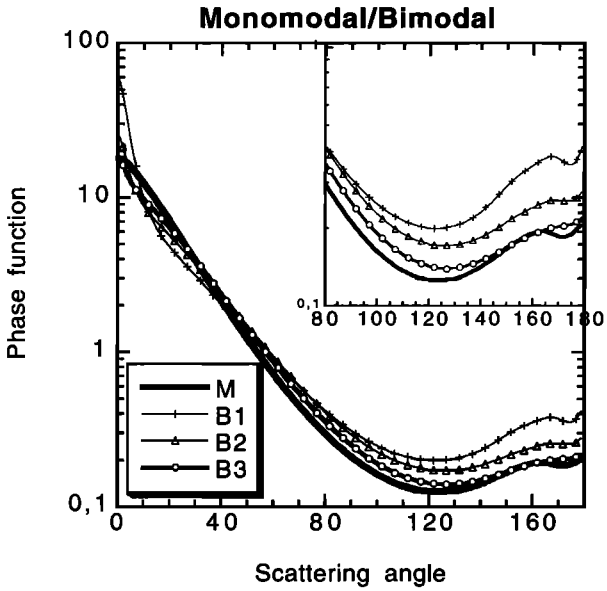

Figure 15. As in Figure 13, but for the phase functions of the monomodal model (M) and of equivalent bimodal models (B). Depending on the choice for the small mode, the phase function of an equivalent bimodal model may exhibit less dissymmetry than the monomodal model one.

side-scattering angles which require aerosol size distributions with two modes when the particles start to be larger. When α decreases, however, either bimodal or monomodal size distributions of spherical particles lead to directional effects larger than those which are observed. Since the upward radiance is more and more representative of the coarse mode of particles when α decreases, the trend of our directional radiances may be explained by assuming that the phase function of the coarse mode of particles is more isotropic than that of spherical particles.

As shown by *Hansen and Travis* [1974], the phase function dissymmetry of large enough spherical particles (say, with effective radius $2\pi r_{\text{eff}}/\lambda \sim 10$ or more) cannot be changed significantly by changing the size distribution or the refractive index of the particles. On the contrary, it is well known that nonspherical particles tend to exhibit nearly isotropic phase function in side-scattering and backscattering directions [see, e.g., *Cai and Liou*, 1982; *De Haan*, 1987; *Brogniez*, 1992; *Masuda and Takashima*, 1992; *Mishchenko and Travis*, 1994a; *Labonnote et al.*, 2000]. The observed trend therefore may be indicative that the large mode of aerosols consists partly of nonspherical particles. Note that this should be consistent also with the systematic lack of large rainbow features in the POLDER measurements, within the range $140° < \Theta < 180°$, since nonsphericity is known to remove the rainbow of spherical particles [see, e.g., *Cai and Liou*, 1982; *De Haan*, 1987; *Brogniez*, 1992; *Masuda and Takashima*, 1992; *Mishchenko and Travis*, 1994a].

To more quantitatively test this assumption of nonspherical particles, the theoretical behavior of $\Delta D/D$ as a function of α was calculated again but substituting a nonspherical coarse mode for the previous coarse model of spherical particles, as suggested by *Mishchenko et al.*'s [1997] model of polydisperse, equiprobable shape mixture of prolate and oblate spheroids of large enough dimensions. Let $p_c^s(\Theta)$ and $p_c^{ns}(\Theta)$ stand for the phase function of the spherical and nonspherical coarse modes, respectively (with $p_c^s(\Theta)$ derived from Mie theory for $\bar{r}_C = 0.80$ μm). We assumed

$$\begin{aligned} p_c^{ns}(\Theta) &= p_c^s(\Theta) \qquad \Theta < 80° \\ p_c^{ns}(\Theta) &= p_c^s(80°) \qquad \Theta > 80° \end{aligned} \tag{10}$$

according to the typical trend of the phase functions for polydisperse large spheroids with $2\pi r_{\text{eff}}/\lambda_0$ larger than ~10 in Plate 5 of *Mishchenko et al.* [1997]. Moreover, the spectral dependence of the scattering coefficient of this nonspherical mode was assumed to be the same as that of the spherical coarse mode, which is a reasonable approximation according to Figure 4 of *Mishchenko et al.* [1997]. The new relationship between $\Delta D/D$ and the Ångström exponent of the monomodal model is shown in Figure 17. The nonspherical model (crosses in Figure 17) leads to a dramatic modification of the behavior of $\Delta D/D$ whose the trend is now consistent with the results in Plate 6. However, the efficiency of this model (100% nonspherical particle case in Figure 17) is 5 to 10 times larger than the effect observed in Plate 6. So in Figure 17 we have also reported results obtained by substituting only 25% and 50% of the previous nonspherical model of particles to the spherical particles of the coarse mode (i.e., with the coarse mode phase function, p_c, given by $p_c = (1 - x)p_c^s + xp_c^{ns}$, with $x = 0.25$ and $x = 0.50$). Despite the crudity of these estimates, the discrepancy in the directional radiance retrieval achieved by the present algorithm could be probably accounted for by assuming an aerosol coarse mode consisting partly, for 10% to 20%, of nonspherical particles. It must be noticed that the pixels corresponding to large values of $\bar{\Delta}L/\bar{L}$ in Plate 6, which are principally relevant of the previous analysis, mostly correspond to desertic dust particles transported over the tropical Atlantic Ocean, for which the sphericity assumption is questionable.

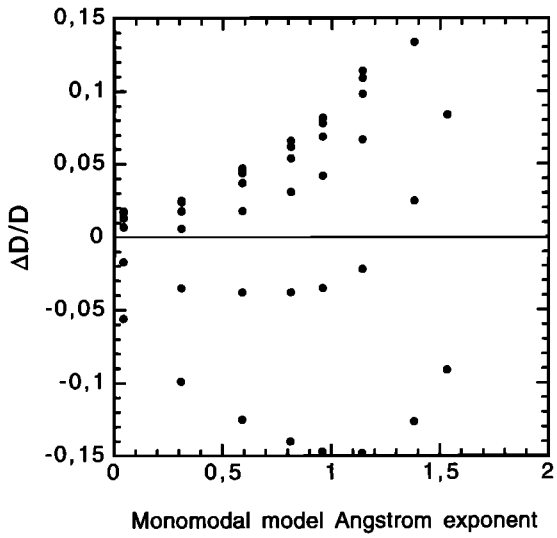

Figure 16. Expected relationship between the Ångström exponent α of the retrieved monomodal model and the discrepancy $\Delta D/D = (D_m - D_b)/D_b$ in the directional radiance retrieval in the presence of aerosols with bimodal size distribution. For different values of α, D_m and D_b are estimates of the phase function dissymmetries for monomodal and equivalent bimodal models which yield the same radiance ratio R, with $D = \bar{p}_{\lambda_0}(160°)/\bar{p}_{\lambda_0}(110°)$ for the estimate of the dissymmetry (see text).

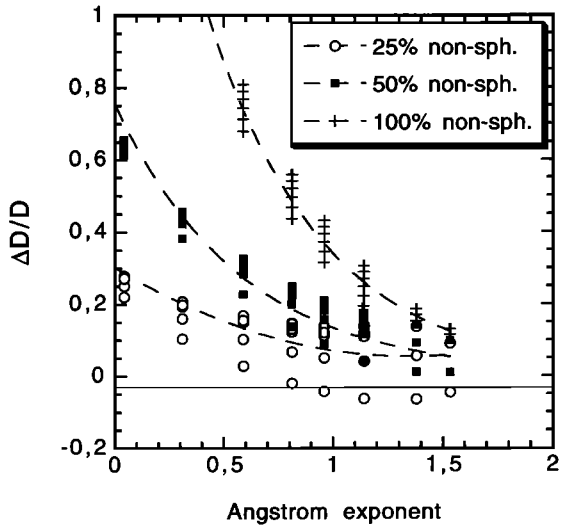

Figure 17. Same as Figure 16 but with the coarse mode of the equivalent bimodal models showing a comparison between the polarized phase function (M) for spherical particles with a monomodal size distribution ($\bar{r}$ = 0.04 μm, σ = 0.8635 in equation (1); m = 1.40).

5. Conclusion

The spectral, directional, and polarized characteristics of the solar radiation observed by POLDER over the oceans have been processed so far assuming spherical nonabsorbing aerosols with monomodal lognormal size distributions. As shown by *Goloub et al.* [1999], the optical thickness and Ångström exponent of the particles derived this way, principally from the radiance measurements, are consistent with ground-based correlative measurements, except for some systematic underestimation of the Ångström exponent by POLDER. The multidirectional and polarized capabilities of POLDER also permit control of the validity of the aerosol models. The present in-depth analysis of the measurements over surface target with favorable observation geometries points out the following general trends.

Small aerosols with Ångström exponents larger than ~1.0 exhibit generally directional and polarized effects consistent with the assumption of a single mode of particles. For such cases, improvement in the retrieval of the particle refractive index will be searched for by simply using an extended set of monomodal models.

As larger and larger particles are present, corresponding to smaller Ångström exponents, monomodal models lead to increasing discrepancies both in the directional and polarized features of the aerosols. Compared with the predictions of monomodal models, the data generally exhibit an aerosol phase function slightly more isotropic in backscattering directions and a much larger polarized phase function in side-scattering directions. The underestimation of the polarized light in side-scattering directions by the theoretical models is an indication of the bimodality of the aerosol size distribution, as previously derived from ground-based radiance measurements [*Remer and Kaufman*, 1998]. Bimodality of the size distribution of spherical particles, nevertheless, seems unable to explain the overestimation of the dissymmetry of the directional radiance by the models. This trend, which is principally observed for Saharan dust, can be explained by assuming a coarse mode consisting partly of nonspherical particles. The systematic lack of a pronounced rainbow feature in the POLDER data would be also consistent with nonsphericity of the large particles. Confirmation of these points requires an improved analysis of the POLDER data and an improved inversion code of the POLDER data based on such bimodal models as presently developed.

Acknowledgments. Results presented in this paper were obtained using data from CNES's POLDER on board NASDA's ADEOS. This study was funded by the Centre National d'Etudes Spatiales (CNES), the Centre National de la Recherche Scientifique (CNRS), the Conseil Régional du Nord-Pas de Calais, the Fonds Européen de Développement Régional (FEDER), and the Délégation Régionale à la Recherche et à la Technologie du Nord-Pas de Calais. The authors would like to acknowledge A. Lifermann, the POLDER Project Scientist, for her constant support. Informations on POLDER data can be found on the following Web site: http://polder@www-projet.cnes.fr:8060.

References

Bréon, F. M., and S. Colzy, Cloud detection from the spaceborne POLDER instrument and validation against surface synoptic observations, *J. Appl. Meteorol.*, *36*, 777–785, 1999.

Brogniez, G., Contribution à l'étude des propriétés optiques et radiatives des cirrus, thèse d'etat, Univ. des Sci. et Technol., Lille, France, 1992.

Cai, Q., and K. N. Liou, Polarized light scattering by hexagonal ice cristals: Theory, *Appl. Opt.*, *21*, 3569–3580, 1982.

Charlson, R. J., S. E. Schwatz, J. M. Hales, R. D. Cess, J. A. Coakley, J. E. Hansen, and D. H. Hofmann, Climate forcing by anthropogenic aerosols, *Science*, *255*, 423–430, 1992.

Cox, C., and W. Munk, Measurements of the roughness of the sea surface from photographs of the Sun's glitter, *J. Opt. Soc. Am.*, *44*, 838–850, 1954.

De Haan, J., Effects of aerosols on the brightness and polarization of cloudless planetary atmospheres, M.S. thesis, Fre Univ. of Amsterdam, Amsterdam, Netherlands, 1987.

Deschamps, P. Y., F. M. Bréon, M. Leroy, A. Podaire, A. Bricaud, J. C. Buriez, and G. Seze, The POLDER mission: Instrument characteristics and scientific objectives, *IEEE Trans. Geosci. Remote Sens.*, *32*, 598–615, 1994.

Deuzé, J. L., M. Herman, and R. Santer, Fourier series expansion of the transfer equation in the atmosphere-ocean system, *J. Quant. Spectrosc. Radiat. Transfer*, *41*, 483–494, 1988.

Deuzé, J. L., M. Herman, P. Goloub, D. Tanré, and A. Marchand, Characterisation of aerosols over ocean from POLDER-ADEOS-1, *Geophys. Res. Lett.*, *26*, 1421–1425, 1999.

Fraser, R. S., Satellite measurement of mass of Sahara dust in the atmosphere, *Appl. Opt.*, *15*, 2471–2479, 1976.

Goloub, P., D. Tanré, J. L. Deuzé, M. Herman, A. Marchand, and F.-M. Bréon, Validation of the first algorithm applied for deriving the aerosol properties over the ocean using the POLDER/ADEOS measurements, *IEEE Trans. Geosci. Remote Sens.*, *37*, 1586–1596, 1999.

Gordon, H. R., and M. Wang, Retrieval of water-leaving radiance and aerosol optical thickness over the oceans with SeaWiFS: A preliminary algorithm, *Appl. Opt.*, *33*, 443–452, 1994.

Hagolle, O., P. Goloub, P. Y. Deschamps, H. Cosnefroy, X. Briottet, T. Bailleul, J. M. Nicolas, F. Parol, B. Lafrance, and M. Herman, Results of POLDER in-flight calibration, *IEEE Trans. Geosci. Remote Sens.*, *37*, 1550–1566, 1999.

Hansen, J. E., and J. W. Hovenier, Interpretation of the polarization of Venus, *J. Atmos. Sci.*, *31*, 1137–1160, 1974.

Hansen, J. E., and A. A. Lacis, Sun and dust versus greenhouse gases: An assessment of their relative roles in global climate change, *Nature*, *346*, 713–719, 1990.

Hansen, J. E., and Travis, Light scaterring in planetary atmospheres, *Space Sci. Rev.*, *16*, 527–610, 1974.

Hayasaka, M. T., T. Nakajima, and M. Tanaka, The coarse particle aerosols in the free troposphere around Japan, *J. Geophys. Res.*, *95*, 14,039–14,047, 1990.

Herman, J. R., P. K. Bhartia, O. Torres, C. Hsu, C. Seftor, and E.

Celarier, Global distribution of UV-absorbing aerosols from Nimbus 7/TOMS data, *J. Geophys. Res.*, *102*, 16,911–16,922, 1997.

Higurashi, A., and T. Nakajima, Development of a two channel aerosol retrieval algorithm on global scale using NOAA/AVHRR, *J. Atmos. Sci.*, *56*, 924–941, 1999.

Holben, B. N., et al., AERONET—A federated instrument network and data archive for aerosol characterization, *Remote Sens. Environ.*, *66*, 1–16, 1998.

Husar, R. B., J. M. Prospero, and L. L. Stowe, Characterization of tropospheric aerosols over the oceans with the NOAA advanced very high resolution radiometer optical thickness operational product, *J. Geophys. Res.*, *102*, 16,889–16,909, 1997.

Kaufman, Y. J., A. Gitelson, A. Karniely, E. Ganor, R. S. Fraser, T. Nakajima, S. Mattoo, and B. N. Holben, Size distribution and scattering phase function of aerosol particles retrieved from sky brightness measurements, *J. Geophys. Res.*, *99*, 10,341–10,356, 1994.

Koepke, P., Effective reflectance of the oceanic whitecaps, *Appl. Opt.*, *23*, 1816–1824, 1984.

Labonnote, L. C., G. Brogniez, M. Doutriaux-Boucher, J. C. Buriez, J.-F. Gayet, and H. Chepfer, Modeling of light scattering in cirrus clouds with inhomogeneous hexagonal monocristals: Comparison with in-situ and ADEOS-POLDER measurements, *Geophys. Res. Lett.*, *27*, 113–116, 2000.

Lafrance, B., and M. Herman, Correction of the stratospheric aerosol radiative influence in the POLDER measurements, *IEEE Trans. Geosci. Remote Sens.*, *36*, 1599–1608, 1998.

Masuda, K., and T. Takashima, Feasability study of derivation of cirrus information using polarimetric measurements from satellite, *Remote Sens. Environ.*, *39*, 45–59, 1992.

Mishchenko, M. I., and L. D. Travis, Light scattering by polydisperse, rotationally symmetric, non spherical particles: Linear polarization, *J. Quant. Spectrosc. Radiat. Transfer*, *51*, 759–788, 1994a.

Mishchenko, M. I., and L. D. Travis, Light scattering by polydispersions of randomly oriented spheroids with size comparable to wavelengths of observation, *Appl. Opt.*, *33*, 7206–7225, 1994b.

Mishchenko, M. I., and L. D. Travis, R. A. Kahn, and R. A. West, Modeling phase functions for dustlike tropospheric aerosols using a shape mixture of randomly oriented polydisperse spheroids, *J. Geophys. Res.*, *102*, 16,831–16,847, 1997.

Morel, P., Optical modeling of the upper ocean in relation to its biogenous water content (case I waters), *J. Geophys. Res.*, *93*, 10,749–10,768, 1983.

Nadal, F., Analyse de la polarisation pour la télédétection de l'atmosphère et des surfaces grâce aux mesures spatiales de POLDER, doctorat, Univ. Paris 7, Méthodes Phys. en Télédétection, Paris, 1999.

Nakajima, T., M. Tanaka, T. Hayasaka, Y. Miyake, Y. Nakanishi, and K. Sasamoto, Airborne measurements of the optical stratification of aerosols in turbid atmospheres, *Appl. Opt.*, *25*, 4374–4381, 1986.

Nakajima, T., A. Higurashi, K. Aoki, T. Endoh, H. Fukushima, M. Toratani, Y. Mitomi, B. G. Mitchell, and R. Frouin, Early phase analysis of OCTS radiance data for aerosol remote sensing, *IEEE Trans. Geosci. Remote Sens.*, *37*, 1575–1585, 1999.

Quenzel, H., and P. Koepke, Tropospheric aerosol optical depth inverted from upwelling radiances, in *Aerosols and Their Climatic Impact*, edited by H. E. Gerber and A. Deepak, pp. 227–240, A. Deepak, Hampton, Va., 1984.

Rao, C. R. N., L. L. Stowe, and E. P. McClain, Remote sensing of aerosols over the oceans using AVHRR data: Theory, practice, and applications, *Int. J. Remote Sens.*, *10*, 743–749, 1989.

Remer, L. A., and Y. J. Kaufman, Dynamic aerosol models: Urban industrial aerosols, *J. Geophys. Res.*, *103*, 13,859–13,871, 1998.

Shettle, E. P., and R. W. Fenn, Models for the aerosols of the lower atmosphere and the effect of humidity variations on their optical properties, *AFGL Tech. Rep.*, *TR-79-0214*, 1979.

Stowe, L. L., R. M. Carey, and P. P. Pellegrino, Monitoring the Mt. Pinatubo aerosol layer with NOAA/AVHRR data, *Remote Sens. Environ.*, *60*, 22–34, 1992.

Tanré, D., C. Deroo, P. Duhaut, M. Herman, J. J. Morcrette, J. Perbos, and P. Y. Deschamps, Description of a computer code to simulate the satellite signal in the solar spectrum, *Int. J. Remote Sens.*, *11*, 659–668, 1990.

Tanré, D., Y. J. Kaufman, M. Herman, and S. Matoo, Remote sensing of aerosol properties over the oceans using the MODIS/EOS spectral radiances, *J. Geophys. Res.*, *102*, 16,971–16,988, 1997.

Torres, O., P. K. Bhartia, J. R. Herman, Z. Ahmad, and J. Gleason, Derivation of aerosol properties from satellite measurements of backscattered ultraviolet radiation: Theoretical basis, *J. Geophys. Res.*, *103*, 17,099–17,110, 1998.

Vesperini, M., F. M. Bréon, and D. Tanré, Atmospheric water vapor content from space-borne POLDER measurements, *IEEE Trans. Geosci. Remote Sens.*, *37*, 1613–1619, 1999.

J. L. Deuzé, P. Goloub, M. Herman, A. Marchand, G. Perry, and D. Tanré, Laboratoire d'Optique Atmosphérique, Université de Lille 1, F-59655 Villeneuve d'Ascq cedex, France. (deuze@loa.univ-lille1.fr)

S. Susana, Laboratoire des Sciences du Climat et de l'Environnement, CEA Saclay, L'orme des Merisiers, F-91191 Gif-sur-Yvette, France.

(Received July 9, 1999; revised January 3, 2000;
accepted February 16, 2000.)